Displacement Damage in Silicon Detectors for High Energy Physics

Michael Moll

Abstract— **In this paper, we review the radiation damage issues caused by displacement damage in silicon sensors operating in the harsh radiation environments of high energy physics experiments. The origin and parameterization of the changes in the macroscopic electrical sensor properties such as depletion voltage, leakage current, and charge collection efficiency as a function of fluence of different particles, annealing time, and annealing temperature are reviewed. The impact of impurities in the silicon base crystal on these changes is discussed, revealing their effects on the degradation of the sensor properties. Differences on how segmented and nonsegmented devices are affected and how device engineering can improve radiation hardness are explained and characterization techniques used to study sensor performance and the electric field distribution inside the irradiated devices are outlined. Finally, recent developments in radiation hardening and simulation techniques using technology computer-aided design modeling are given. This paper concludes with radiation damage issues in presently operating experiments and gives an outlook of radiation-hardened technologies to be used in the future upgrades of the Large Hadron Collider and beyond.**

Index Terms— **Clusters, defects, displacement damage, nonionizing energy loss (NIEL), particle detectors, radiation effects, semiconductors, silicon, simulation, technology computer-aided design (TCAD).**

I. Introduction

DETECTORS used in high energy physics (HEP) experiments are often operating in high particle-flux environments, which are required to obtain the large statistical samples needed to characterize rare physics processes. The present installed detectors in the Large Hadron Collider (LHC) at CERN cumulated radiation levels over the anticipated lifetime (an integrated luminosity of 300 fb^{-1}) of about 2×10^{15} n_{eq}/cm^2 and ionizing doses of about 300 kGy for the innermost pixel sensors are to be expected. For the High-Luminosity LHC (HL-LHC), the upgrade of the LHC coming to operation in 2026, a more than 10 times higher integrated luminosity of 4000 fb^{-1} with corresponding more than 10 times higher radiation levels is anticipated [1]. In comparison to radiation fields encountered in space applications, the displacement damage effects, i.e., the effects arising from the dislocation of lattice atoms from their normal lattice sites by energetic radiation, in high luminosity accelerator experiments are in higher orders of magnitude. The radiation fields in the experiments of the LHC are, therefore, unique in terms of intensity and composition.

While results obtained in the low particle fluence range for non-HEP applications can partly be applied to HEP technology, the operation of semiconductor devices in the high-fluence range has called for dedicated R&D programs [2]–[5]. The aim is to understand displacement damage effects on semiconductor devices, and in particular silicon detectors, and to perform targeted radiation testing campaigns and technology developments to assure a proper performance over decades of operation in the harsh radiation environments of the experiments.

Recent review articles and books with relevance for displacement damage in silicon devices for HEP applications have been published by Kramberger [6], Leroy and Rancoita [7], Srour and Palko [8], and Hartmann [9].

In the following, we briefly summarize the present plans for silicon devices in the future experiments in the HL-LHC and the future circular collider (FCC) (Section I-A), review the radiation fields in HEP experiments (Section I-B), the nonionizing energy loss (NIEL) scaling (Section I-C), and the impact of defects on sensor performance (Section I-D)x. These subjects are treated in view of their relevance for the understanding of the material presented on displacement damage in silicon detectors in Sections II–VII.

A. Detector Upgrades and Radiation Fields in HEP Applications

The increased instantaneous and integrated luminosity anticipated for the HL-LHC [1], [10] leads in the need to cope with higher particle fluxes per bunch crossing and increased radiation levels. This calls for finer granularity in the sensing elements, faster front-end electronics and data transfer, reduced mass, new triggering and cooling concepts, and more online/offline computing power and has, for example, led to the wish to employ high-precision timing detectors allowing to distinguish between interactions of the same bunch crossing but with a tiny difference in interaction time in the order of tens of picoseconds. The present roadmap toward the HL-LHC is shown in Fig. 1. The schedule shows the operational periods of the LHC and HL-LHC, which are interleaved with extended year-end technical stops for maintenance and preparatory works and long shutdowns (LS) in

Manuscript received October 31, 2017; revised February 7, 2018; accepted March 12, 2018. Date of publication April 4, 2018; date of current version August 15, 2018.

The author is with the Experimental Physics Department, CERN, 1211 Geneva, Switzerland (e-mail: michael.moll@cern.ch).

Color versions of one or more of the figures in this paper are available online at http://ieeexplore.ieee.org.

Digital Object Identifier 10.1109/TNS.2018.2819506

Fig. 1. Schedule of the LHC and HL-LHC projects (status July 2017) [10].

which new detector and accelerator components are installed. Major upgrades for the ALICE [12] and LHCb [11] experiments will take place in LS2 while the major upgrades for ATLAS [13] and CMS [16] fall into LS3. Focusing on the most significant upgrades involving silicon detectors, the following activities shall be mentioned: In LS2 (2019–2020), the LHCb Vertex Locator (VELO) detector will be replaced going from the present strip sensor concept toward a pixel sensor with 55 μm $\times$ 55 μm pixels and the trackers [trigger tracker and upstream tracker] evolve toward higher granularity and thinner strip sensors [11]. A new scintillating fiber tracker will be equipped with silicon photomultipliers that will have to be operated cold to cope with the radiation levels. In ALICE, a new inner tracking system will be installed in LS2 using monolithic active pixel sensors with 30 μm $\times$ 30 μm pixels [12]. In LS3 (2024–2026), the ATLAS and CMS inner tracking detectors will be replaced [13]–[17]. The silicon strip sensors in the upgraded trackers will consist of n-type strips in p-type substrates (n-in-p) and replace the previously used (p-in-n) technology. This is driven by radiation hardness considerations, as it was demonstrated that ionizing and displacement damage have a less detrimental impact on detector performance for n-in-p devices than for p-in-n devices (see Section III-B). For the pixel detector layers, various sensor options are feasible with thin planar n-in-p sensors bump-bonded to the readout application-specified integrated circuit (hybrid pixel detectors) being the baseline solution, replacing the previously used n-in-n sensor technology. Other sensor options are 3-D silicon sensors and complementary metal–oxide–semiconductor (CMOS) sensors. While 3-D sensors have, very recently, become the baseline sensor concept for the innermost pixel layer of the ATLAS phase-2 upgrade [15], CMOS sensors are still under development. In CMS, the hadronic endcap calorimeters will be replaced as they suffer from radiation damage. The replacement is called the high granularity calorimeter (HGCAL) [18] and will consists of 28 silicon planes in its electromagnetic compartment (CE-E), 24 silicon planes in the hadronic

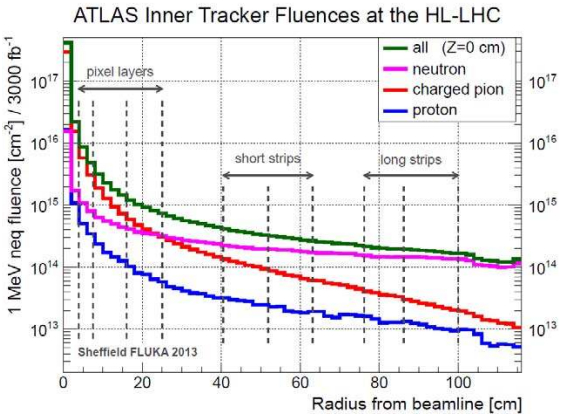

Fig. 2. Expected fluences of particles in the inner tracker of the ATLAS detector at HL-LHC for an integrated luminosity of 3000 fb^{-1}. Figure taken from [19].

compartment (CE-H), and mixed silicon/scintillator planes interleaved with absorber layers. The silicon detectors are pad sensors (0.5 or 1.2 cm^2) of different thicknesses (120 to 300 μm) depending on the radial position and according to the expected cumulated radiation levels which reach from 2×10^{14} n_{eq}/cm^2 to about 10^{16} n_{eq}/cm^2. They cover a surface of about 500 m^2 and are operated at -30 °C to limit the impact of radiation damage.

B. Radiation Fields

The anticipated radiation levels for the HL-LHC ATLAS inner tracker in units of 1-MeV neutron equivalent fluence (n_{eq}, see Section I-C) after an integrated luminosity of 3000 fb^{-1} are shown in Fig. 2 and are very similar to the expected fluence levels for the HL-LHC CMS Tracker. The expected cumulated particle fluence at the center of the detector ($z = 0$ cm, interaction point) is plotted against the radius of the detector. The anticipated positions for the various layers of the ATLAS pixel and strip detectors are indicated in the plot. Close to the beam pipe, at a radius of 3.8 cm, a fluence of up to about 1.5×10^{16} n_{eq}/cm^2 and 8 MGy is

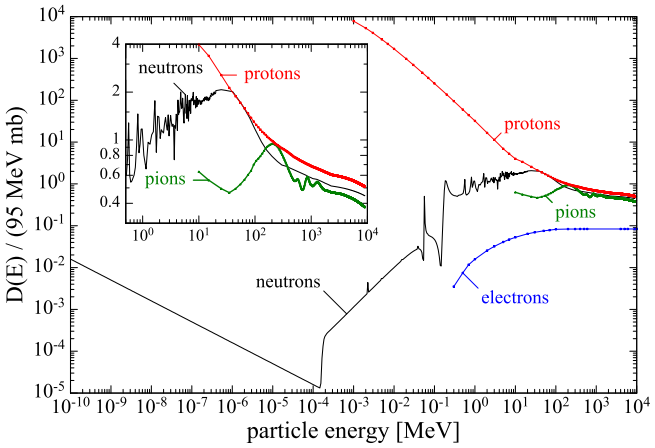

Fig. 3. NIEL cross sections normalized to 95 MeV mb. Data collected by A. Vasilescu and G. Lindstroem [22] based on [23]–[26] and private communications.

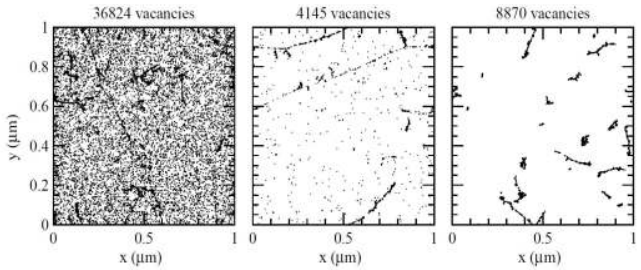

Fig. 4. Initial distribution of vacancies produced by 10-MeV protons (left), 23-GeV protons (middle), and 1-MeV neutrons (right). The plots are projected over 1 μm depth (z) and correspond to a fluence of 10^{14} particles/cm^2. Figure taken from [27].

expected for pixel sensors, while for the innermost strip sensor layers at 40 cm radius up to about 5×10^{14} n_{eq}/cm^2 and 200 kGy are expected [19]. An important aspect regarding the particle spectrum is the fact that for the pixel layers, the charged hadron component (mainly charged pions) is dominating, while for the outer layers the neutron component is dominating. It will be demonstrated in Section II-C that the type of particle (i.e., charged hadron damage versus neutron damage) has an important impact on the radiation-induced degradation of the sensor performance. At a much longer time scale, a 100-TeV center-of-mass energy proton-proton collider in a ≈100-km-long tunnel is investigated within the FCC project study [20]. Radiation levels in a corresponding detector will go up to two orders of magnitude beyond the radiation levels expected for the HL-LHC detectors. Assuming a cumulated luminosity of 30 ab^{-1}, a fluence of $\approx 6 \times 10^{17}$ n_{eq}/cm^2 and 400 MGy will be reached for inner pixel layers at 2.5 cm radius [21]. These are unprecedented radiation levels which are going well beyond radiation damage studies performed so far, and thus, are calling for an in-depth evaluation program of the displacement damage induced by these enormous levels of radiation on sensors and other detector components.

C. Nonionizing Energy Loss

The NIEL gives the portion of energy lost by a traversing particle which does not go into ionization and eventually leads to displacement damage. However, only a fraction of the NIEL leads to displacements as a part of the energy dissipated in phonons. This fraction depends on the energy of the impinging particle. NIEL is defined in units of MeVcm^2/g or as NIEL cross section (displacement damage function D) in units of MeVmb. A reference value of 1-MeV neutron equivalent (n_{eq}) has been fixed to 95 MeVmb. Calculated values of NIEL cross sections for various particles are shown in Fig. 3.

The NIEL hypothesis assumes that radiation damage effects scale linear with NIEL irrespective of the distribution of the primary displacements over energy and space. For the simulated examples shown in Fig. 4, the number of vacancies should give a measure of the damage irrespectively of their distribution, whether homogeneously scattered over a relatively wide volume (like for the case of low-energetic proton or gamma-ray damage) or clustered in high density in small regions (like in the case of neutron damage).

Consequently, the damage produced by different particles or particles with different energy should be scalable via their NIEL (i.e., the number of displacements) and the data given in Fig. 3 should allow to normalize the damage from different particles or particles with different energies to each other. As will be shown in the following, NIEL scaling is a powerful method for coping with displacement damage predictions in complex radiation fields. It allows to predict many device damage parameters in fast-hadron-dominated radiation fields (e.g., the leakage current) but also has shortcomings arising, for example, from the fact that pointlike and clustered defects contribute differently to some device damage parameters such as the effective space charge (see Section I-D). The displacement damage functions, shown in Fig. 3, are presently used to calculate the 1-MeV neutron equivalent fluence radiation fields in the experiments of the LHC and HL-LHC. It has, however, been shown that for protons and electrons, an *effective NIEL* [28], [29] or the *equivalent displacement damage dose* concept [29]–[31] can deliver better linearity between some damage parameters and the calculated NIEL (see [32]). A revision of the used damage functions for the 1-MeV neutron equivalent fluence calculation is thus of interest.

D. Impact of Defects on Silicon Sensors

Radiation-induced electrically active defects with energy levels in the silicon bandgap impact on the device performance in various ways. Generally, the impact on the detector performance can be described in the framework of the Shockley–Read–Hall (SRH) statistics and in principle the impact of each defect can be calculated, if the capture cross sections for holes σ_p and electrons σ_n, the position in the bandgap, the type of defect (acceptor or donor), and the concentration of the defect N_t are known (see [33]). On the device performance level, three main effects can be identified and are discussed in the following with their formulation in the SRH framework.

1) Leakage Current: The leakage current is most effectively produced by defect levels close to the middle of the bandgap and follows the NIEL hypothesis scaling for hadron damage,

meaning as well that defect engineering (i.e., impurity content of the silicon) has no impact (see Section II-B). Increase of leakage current leads to an increase of noise in the amplifiers and to an increase of power consumption. As the leakage current depends exponentially on the temperature, cooling is a very effective means to mitigate the detrimental effects. To calculate the leakage current, we need to determine the defect occupancy with electrons f_t given as

$$f_t = \frac{c_n n + e_p}{c_n n + e_n + c_p p + e_p} \tag{1}$$

where c_n and c_p are the capture coefficients for electrons and holes, n and p are the electron and hole densities, and e_n and e_p are the emission rates for electrons and holes. c_n is given by $c_n = \sigma_n \upsilon_{\text{th},n}$ with $\upsilon_{\text{th},n}$ being the thermal velocity for electrons and e_n is given by $e_n = c_n n_i \exp((E_t - E_i)/k_B T)$ with n_i being the intrinsic carrier density, E_i is the intrinsic fermi level, and k_B is Boltzmann's constant. In the space charge region (SCR) of a detector, the carrier densities are very low and can often be neglected simplifying (1) to become

$$f_t = e_p/(e_n + e_p). \tag{2}$$

Defect levels are producing leakage current by the subsequent emission of electrons and holes (i.e., the transfer of electrons from the valence to the conduction band). The generation rate G_t of a single defect type t in the case of neglectable free carrier concentrations is given as

$$G_t = N_t f_t e_n = N_t (1 - f_t) e_p = N_t \frac{e_n e_p}{e_n + e_p}. \tag{3}$$

Summing over all defect types and taking into account the active volume of a sensor (depletion width w and area A) results into the total leakage of the device

$$I = q_0 w A \sum_{\text{defects}} G_t \tag{4}$$

with q_0 being the elementary charge.

2) Effective Space Charge: In undamaged sensors, the bulk doping (e.g., phosphorus or boron) constitutes the effective space charge. Radiation-induced changes to the effective space charge lead to a change of the electric field distribution within the device and shift the depletion voltage to lower or higher values. In the latter case, higher operation voltages might have to be applied to establish an electric field throughout the full sensor volume in order to avoid underdepletion and loss of active volume, and therefore signal. If sufficiently high voltage (HV) cannot be applied or breakdown of the sensor is at risk, sensors will have to be operated underdepleted with the corresponding loss in signal heights. Inhomogeneous distribution of space charge might lead to double junction effects or the shift of the highest electric field toward regions that are unprofitable for segmented sensors. High local fields can lead furthermore to impact ionization effects or breakdown. It has been shown that the change of the space charge in silicon is strongly material-dependent (e.g., oxygen content) and depending on the particle type used for the irradiation experiment (e.g., neutron versus proton damage). This implies that this damage effect does not directly scale with NIEL and can be altered or mitigated by defect engineering approaches (e.g., change of impurity content). Defects can contribute with positive (donors) or negative (acceptors) charge to the space charge, and thus, alter the electric field distribution and the depletion voltage of a device. The effective space charge N_{eff} (neglecting free carriers) is then given by the sum of all positively charged donors N_D and all negatively charged acceptors N_A

$$N_{\text{eff}} = \sum_{\text{donors}} (1 - f_t) N_t - \sum_{\text{acceptors}} f_t N_t \tag{5}$$

where the index t is running over all donor and acceptor such as defect types t with concentration N_t.

3) Trapping: Charge carriers generated by ionizing particles or photons in the SCR travel toward the electrodes and constitute the sensor signal. Defect levels can capture (trap) charge carriers, and if the release (detrapping) time of the charge carriers is long compared with the collection time of the system or if the concentration of defects (trapping centers) is very high, the overall signal of the sensor is reduced. Trapping becomes the limiting factor for high-fluence applications. Mitigation of this problem is possible through device modifications leading to faster collection times (i.e., device engineering). In segmented sensors, the collection of electrons instead of holes at the sensing electrodes can be an advantage due to the higher mobility of electrons and the possibility to exploit charge multiplication by impact ionization in lower fields and without device breakdown. The trapping is characterized by a trapping time (inverse capture rate) τ_e for electrons and τ_h for holes that are calculated as

$$1/\tau_e = c_n (1 - f_t) N_t \text{ and } 1/\tau_h = c_p f_t N_t. \tag{6}$$

Summing over all defects contributing to the trapping results into the effective trapping times τ_{eff} for electrons and holes

$$\frac{1}{\tau_{\text{eff,e}}} = \sum_{\text{defects}} c_{(n,t)} (1 - f_t) N_t \tag{7}$$

$$\frac{1}{\tau_{\text{eff,h}}} = \sum_{\text{defects}} c_{(p,t)} f_t N_t. \tag{8}$$

Equations (1)–(8) allow us to estimate the impact of defects (with known parameters donor/acceptor, σ_n, σ_p, E_t, and N_t) on the space charge, current generation, and trapping. For precise calculations, the defect parameters have to be properly embedded in the Poisson and transport equations as, for example, done in technology computer-aided design (TCAD) device simulations (see Section V). This allows to come up for the device geometry, spacial distribution of defect concentrations, free carrier densities, field strength, and other semiconductor effects like, for example, impact ionization.

II. Basic Radiation Effects in Sensors and Their Parameterization

In this section, we review the basic radiation damage effects on silicon detectors as observed on simple diode structures. We are focusing on displacement damage radiation effects as introduced by heavy particles and exclude damage introduced by gamma irradiation or low-energy electrons (i.e., damage

that on the microscopic level is dominated by point defects in the crystal lattice). The latter is significantly different and usually cannot be described by applying a single NIEL hypothesis-based scaling factor to the damage produced by heavy particles in the same device. An example for this difference will be given in the following for the radiation-induced leakage current.

A. Basic Characterization Methods

Silicon particle detectors are basically reverse biased diodes. The most simple test structure to investigate the properties of a silicon detector is, therefore, a so-called *pad detector*. It consists of a large front electrode (with respect to the thickness of the silicon bulk) surrounded by one or a series of guard rings (to protect the collecting electrodes from unwanted currents originating from the edges and to precisely define the active volume) and a homogeneous electrode covering all backside. For n-type bulk structures, the front contact and guard rings are p^+ implant and the backside implant is an n^+ implant. Typical dimensions are 5 mm $\times$ 5 mm for the front electrode and 300 μm for the thickness of the silicon bulk. Most of the results presented in Section II are based on measurements on pad detectors. Segmented sensors add more complexity to the impact of bulk (and surface) radiation damage and will be treated in Section III.

B. Leakage Current

Radiation-induced defect levels close to the middle of the bandgap are very efficient charge carrier generation centers that lead to an increase of the *leakage current* of silicon devices. This current is also called *generation current* or *dark current*. The experimental determination of the leakage current requires a great care to properly determine the semiconductor volume contributing to it, avoiding or subtracting parasitic currents contributed by the device surface or other interfaces, and accurately determine the temperature of the silicon and the annealing state of the device under test.

1) Fluence Dependence: After exposure to highly energetic particles having sufficient energy to produce defect clusters (see Section IV-B), the radiation-induced increase of the leakage current is proportional to the particle fluence and independent of the type, resistivity, and impurity content of the used silicon material [8], [34]. Fig. 5 shows data obtained on various silicon detectors irradiated in a neutron field with 5.2-MeV mean energy and measured at room temperature after a dedicated annealing of 80 min at 60 °C [35]. The proportionality factor is called *current-related damage factor* α and is defined as

$$\alpha = \frac{\Delta I}{V \phi_{\text{eq}}} \tag{9}$$

where ΔI is the leakage current increase caused by irradiation, V is the volume contributing to the current, and ϕ_{eq} is the particle fluence. The data shown in Fig. 5 result in a value of α (80 min, 60 °C) $= (3.99 \pm 0.03) \times 10^{-17}$ A/cm for the measurements taken at 20 °C.

It shall be mentioned that for irradiations producing predominantly point defects (see Section IV-B), a nonlinear

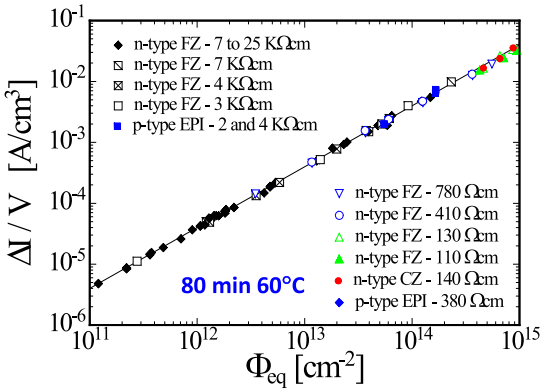

Fig. 5. Radiation induced leakage current increase as function of particle fluence for various silicon detectors made from silicon materials produced by various process technologies with different resistivities and conduction type. The current was measured after a heat treatment of 80 min at 60 °C and is normalized to the current measured at 20 °C. Figure taken from [35].

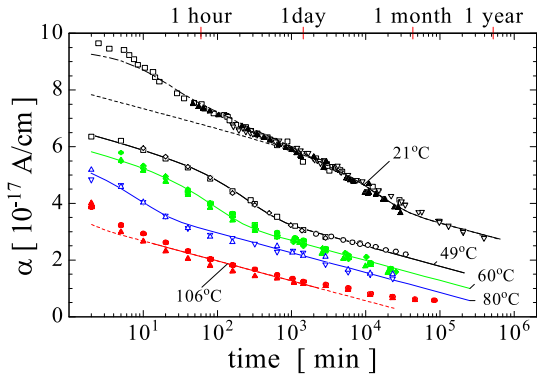

Fig. 6. Current-related damage rate α as a function of cumulated annealing time at different temperatures. Solid lines: fits to the data (see text). Figure taken from [39].

dependence on the particle fluence and a strong dependence on the impurity content are observed [36]. It was found that for gamma-irradiated silicon, the amount of leakage current depends on the oxygen concentration in the material and has quadratic dose (i.e., photon fluence) dependence. The origin of this behavior was attributed to the formation of an oxygen-related point defect called I_p [37].

2) Temperature Dependence: The temperature dependence of the leakage current is dominated by the position of the energy levels in the band gap, their cross sections, their concentrations, and the temperature dependence of the bandgap itself. The most efficient generation centers are the ones at the intrinsic energy level. In this case, the leakage current temperature dependence will follow one of the intrinsic carrier concentrations n_i. In a recent work, Chilingarov [38] compared experimental results obtained on several different irradiated silicon particle detectors using the parameterization $I(T) \propto T^2 \exp(-E_{\text{eff}}/2k_BT)$ and obtained a value of $E_{\text{eff}} = 1.214 \pm 0.014$ eV. This value is presently the reference in the HEP community for temperature correction (scaling) of the leakage current. In practice, this value translates into a reduction of the leakage current by 8%–10% per degree centigrade in the temperature range from room temperature (RT) to −20 °C.

3) Annealing Effects and Parameterization: The annealing behavior of the current-related damage factor α after irradiation is displayed in Fig. 6 for various annealing temperatures ranging from 21 °C to 106 °C [39]. The annealing temperature is the temperature at which the samples are stored or heated to accelerate the defect reactions in the silicon bulk. This temperature shall not be confused with the measurement temperature of the leakage current which in the given example is 20 °C. The α value is continuously decreasing with increasing annealing time. In [35] and [39], a parameterization of the data with an exponential and logarithmic term is proposed

$$\alpha = \alpha_1 \cdot \exp(-t/\tau_1) + \alpha_0 - \alpha_2 \cdot \ln(t/t_0) \tag{10}$$

and has been used in Fig. 6 to fit the data (solid lines). The complete parameter set (α_0, α_1, α_2, τ_1, and t_0) and a discussion on the physics meaning of the parameters can be found in [35] and [39].

C. Space Charge-Effective Doping Concentration

The radiation-induced defects lead to a change in the effective space charge N_{eff} that is reflected in a change of the depletion voltage V_{dep} of silicon detectors. The depletion voltage V_{dep} is given as

$$V_{\text{dep}} = \frac{q|N_{\text{eff}}|d^2}{2\epsilon\epsilon_0} \tag{11}$$

where d is the thickness of the device, q is the elementary charge, ϵ is the relative permittivity of silicon, and ϵ_0 is the vacuum permittivity. It shall be noted that (11) is assuming a constant space charge over the volume of the damaged detector, which is not always the case [40]. Furthermore, the depletion voltage is usually determined from capacitance versus voltage (C–V) measurements at ≈10 kHz and a temperature between +20 °C and −20 °C depending on measurement limits set by the high leakage currents, while a dependence of the depletion voltage on the measurement frequency and temperature has been reported for damaged detectors [41]. It is thus understood that the following parameterizations give precise values for the prediction of the depletion voltage (i.e., the kink in the C–V measurement of a diode), while the translation into N_{eff} via (11) might be afflicted with systematic errors. It shall be mentioned that in highly irradiated detectors, contrary to undamaged detectors, the space charge is no longer identical to the free carrier concentration in thermal equilibrium. Results of characterization methods determining the free carrier density or the low-voltage resistivity are, therefore, not easily correlated with the space charge determined from full depletion voltage (also see Section II-D).

1) Fluence Dependence: Fig. 7 shows an example of the evolution of the effective space charge (i.e., depletion voltage) for an n-type sensor with particle fluence [42]. Before irradiation, the sensor was of high-resistivity n-type (phosphorus-doped) base material resulting in a positive space charge of some 10^{11} cm^{-3}.

Irradiation of the sensor results in the formation of negative space charge which compensates the initial positive space charge. With increasing particle fluence, the net space charge

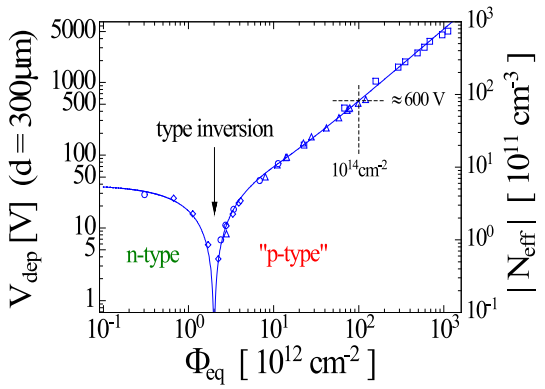

Fig. 7. Effective doping concentration (depletion voltage) as a function of particle fluence for a standard FZ n-type silicon detector. Data were measured directly after exposure and are taken from [42].

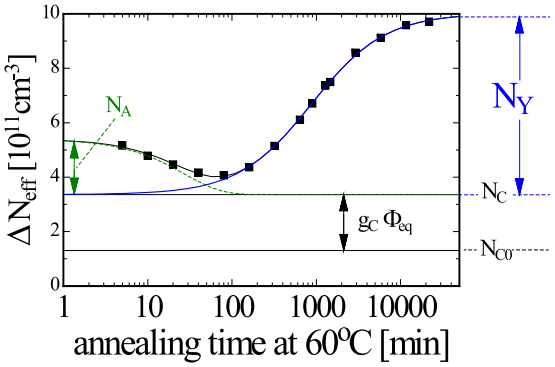

Fig. 8. Evolution of the effective doping concentration as a function of annealing time. The data shown here were taken at room temperature while the annealing took place at 60 °C. Taken from [35].

decreases and reaches very low values corresponding to almost intrinsic silicon. This point is called *type inversion* or *space charge sign inversion (SCSI)* as the space charge sign changes from positive to negative. Increasing the particle fluence beyond the SCSI point leads to more and more negative space charge values. The depletion voltage rises accordingly and eventually reaches values that cannot be applied to the detector any more without causing breakdown. The applied voltage will have to be kept below the depletion voltage and the detector is operated underdepleted. For high-resistivity p-type sensors, no type inversion is usually observed as the initial space charge is already negative before irradiation. It should, however, be mentioned that after neutron and charged-hadron irradiations cases have been observed in nonstandard floating zone (FZ) silicon materials where type inversion occurs from negative to positive space charge [35] or the effective space charge remains positive in n-type sensors up to very high particle fluences [43], [44].

2) Annealing and Parameterization: The effective doping concentration after irradiation is changing with time. This so-called annealing can be accelerated at elevated temperatures and decelerated or frozen when going to lower temperatures. Fig. 8 shows an example for a typical annealing behavior after high-fluence irradiation. The change of the effective doping concentration with irradiation ΔN_{eff} is given as

$$\Delta N_{\text{eff}} = N_{\text{eff},0} - N_{\text{eff}}(t) \tag{12}$$

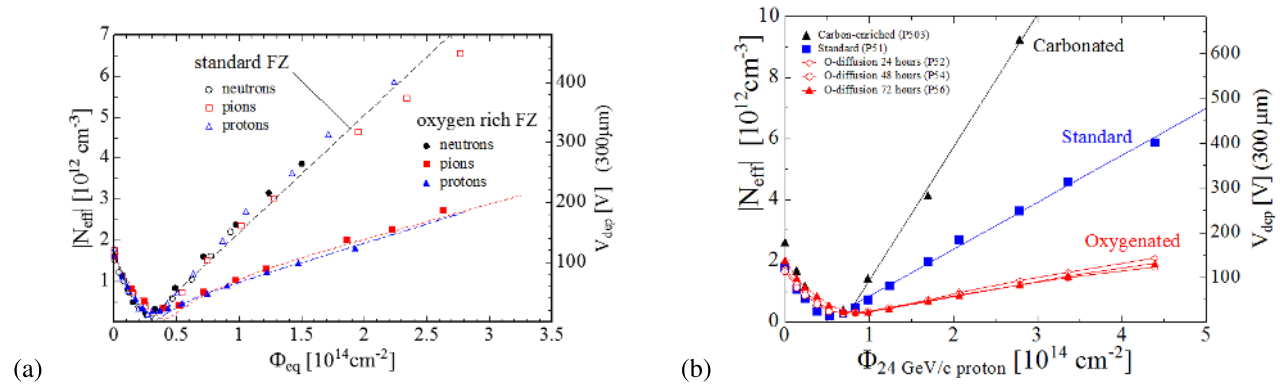

Fig. 9. (a) Dependence of N_{eff} on the accumulated 1-MeV neutron equivalent fluence for standard and oxygen-enriched FZ silicon irradiated with reactor neutrons, 24-GeV/c protons and 192-MeV pions. (b) Effective space charge density and full depletion voltage versus proton fluence for standard, carbon enriched, and three types of oxygen diffused samples: 24, 48, and 72 h diffusion at 1150 °C. Data of the RD48 collaboration taken from [45].

where $N_{\text{eff},0}$ is the value before irradiation and $N_{\text{eff}}(t)$ is the value after irradiation. The fact that ΔN_{eff} is positive for the data shown in Fig. 8 demonstrates that the radiation-induced change of N_{eff} has a negative sign, i.e., the overall produced space charge due to radiation is a negative one in accordance with the data shown in Fig. 7. The time dependence of N_{eff} can be parameterized as

$$\Delta N_{\text{eff}}(t) = N_A(t) + N_C + N_Y(t) \tag{13}$$

where N_C is the so-called *stable damage* component which is not changing with time after irradiation, N_A is the *short term* or beneficial annealing component, and N_Y is the *reverse annealing* component. They are parameterized as

$$N_A(t) = g_a \phi_{\text{eq}} \exp(-t/\tau_a) \tag{14}$$

$$N_C = N_{C,0}(1 - \exp(-c\phi_{\text{eq}})) + g_c \phi_{\text{eq}} \tag{15}$$

$$N_Y(t) = g_y \phi_{\text{eq}}(1 - \exp(-t/\tau_y)) \tag{16}$$

where $N_{C,0}$ represents the fact that often an incomplete doping removal is observed (i.e., $N_{C,0}$ represents only a fraction of the initial doping concentration, see [46]), c is the removal coefficient, and g_a, g_c, and g_y are the introduction rates for the space charge defined as the beneficial annealing, the stable damage, and the reverse annealing above (e.g., $N_Y = g_y \phi_{\text{eq}}$). The temperature dependence of the time constants for the beneficial (τ_a) and the reverse annealing (τ_y) has been found to follow an Arrhenius equation with an activation energy of 1.09 and 1.33 eV, respectively [35]. Note as well that there are different parameterizations for the reverse annealing represented here by (16) (see [35], [43], [46]).

3) Material and Particle Dependence: Material and defect engineering are mitigation techniques that have been extensively used by the the RD48 [4] and RD50 [5] research collaborations. A wide range of sensors produced on different silicon base materials (e.g., different growth methods or different impurity contents), exposed to different types of particles (e.g., electrons, pions, protons, and neutrons) and tested under various operational conditions (e.g., different temperatures and/or applied voltages during and after irradiation) have been studied. These studies demonstrated that the impurity content of the used silicon and the type of particle used for the irradiation experiment have a strong impact on the observed radiation damage, or more precisely, on the space charge and the electric field distribution within the sensor. This is, on the one hand, not in accordance with the NIEL hypothesis described in Section I-C, but on the other hand opening the road toward defect and material engineering for radiation damage mitigation. Extensive—and most successful—studies were performed on materials with different oxygen contents. The variation of oxygen concentration was partly obtained using silicon produced by different growth techniques [FZ, epitaxial, Czochralski or magnetic Czochralski (MCz), and partly by postprocessing of the silicon wafers by long oxidation: diffusion-oxygenated FZ (DOFZ) or diffusion-oxygenated epitaxial (EPI-DO)]. A wide range of impurities was incorporated into the silicon base material as well (carbon, hydrogen, nitrogen, and others) and the corresponding sensors tested in terms of their radiation hardness. Fig. 9 shows an example of data [45] obtained on various n-type silicon detectors in a so-called *CERN scenario measurement* technique [47] where individual samples are successively exposed to radiation with annealing steps and measurements in between each irradiation step. The minimum in the curves for $|N_{\text{eff}}|$ is displaying the fluence for which the material undergoes SCSI from positive to negative space charge from where-on the increase at higher fluence values is almost linear. The slope of this branch is a measure of the radiation hardness. Although oxygenated material does not exhibit any benefit for neutron irradiation [see Fig. 9(a)], it clearly leads to superior results with respect to the standard FZ silicon in case of proton- or pion-induced damage. While the improvement in slope is about a factor of three for oxygen-enriched material, an adverse effect is found for carbon enrichment [see Fig. 9(b)]. Following the developments of the RD48 collaboration, the ATLAS and CMS pixel detectors at the LHC have been made from oxygen-enriched silicon.

D. Acceptor and Donor Removal

From the term acceptor (donor) removal, we understand the transformation of electrically active shallow acceptors (donors) into defect complexes that are no longer having the properties of those shallow dopants. The negative (positive)

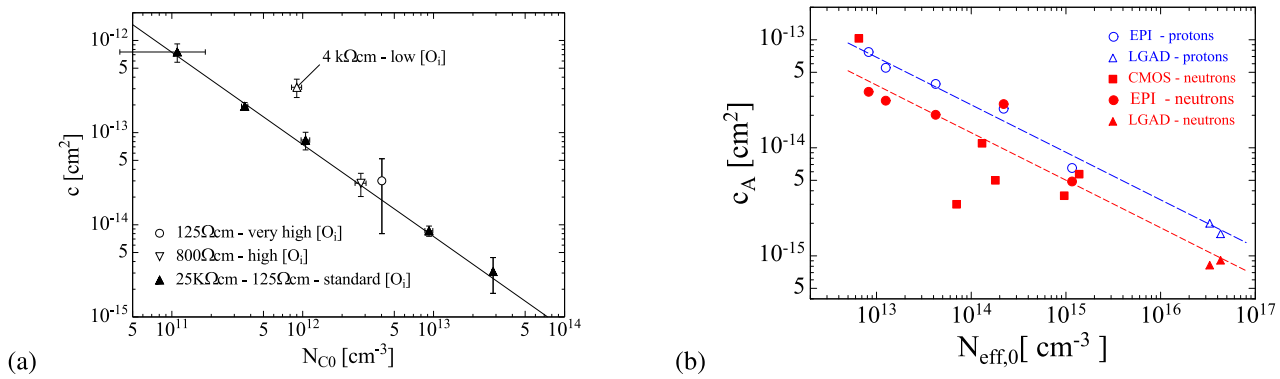

Fig. 10. (a) Donor removal coefficient c_D plotted versus the donor concentration N_{c0} [46]. (b) Acceptor removal coefficient c_A plotted versus the acceptor concentration of the nonirradiated device. Data for proton and neutron irradiated LGAD, sensors made from EPI silicon and CMOS sensors are given [48]–[54]. The lines are guides to the eye indicating that after proton irradiation a higher value of c_A is observed as compared to neutron irradiation.

space charge contributed by the shallow dopants is, therefore, lost and the overall space charge is altered. Experimentally, the removal process is, for example, characterized by the change of the depletion voltage of silicon diodes as a function of irradiation fluence (see Section II-C). It should, however, be mentioned that this is only an indirect measurement of the process, assuming that: 1) the depletion voltage can be transferred into effective space charge by (11) and 2) the observed *donor/acceptor removal component* in the parameterization given in Section II-C is entirely due to the physical removal process of the shallow dopants. Another approach is to measure the change in resistivity of a material, i.e., to measure the free carrier concentration. This approach is assuming that the free carrier concentration is entirely corresponding to the shallow dopant concentration, which in highly irradiated (i.e., highly compensated) material is no longer true as also other defects than those related to the shallow dopants can reduce the free carrier concentration. This method is, therefore, less reliable for characterizing the removal processes and should be treated with care. The removal of phosphorus and boron by irradiation with fast neutrons has been measured by Wunstorf *et al.* [55] using different high-resistivity silicon wafers that were partly doped by the neutron transmutation doping technique. From the measurement of the resistivity change as function of neutron fluence removal coefficients were determined to be $c_D = 2.4 \times 10^{-13}$ cm^2 for phosphorus and $c_A = 2.0 \times 10^{-13}$ cm^2 for boron in very high-resistivity p-type and n-type materials (>1 kΩcm). A systematic investigation of the dependence of the donor removal coefficient determined from space charge measurements on the phosphorus content (material resistivity) [46] revealed that the product of removal coefficient and phosphorus concentration gives a constant value for materials varying over several orders of magnitude in resistivity, as shown in Fig. 10(a). Assuming an exponential decrease of the initial doping concentration $N_{D,0}$ as parameterized earlier, we can approximate to small fluences as

$$N_D(\phi) = N_{D,0} \exp(-c_D \phi) \approx N_{D,0} - c_D N_{D,0} \phi. \quad (17)$$

For small fluences, the term $c_D N_D$ gives the initial doping removal rate that multiplied with the fluence should result in the absolute number of removed doping atoms. A value

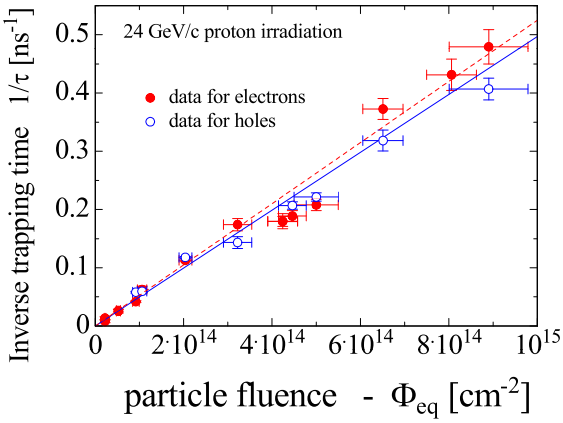

Fig. 11. Inverse trapping time as function of particle fluence as measured at 0 °C after an annealing of 30 to 60 min at 60 °C. Data taken from [56].

of ≈0.1 cm^{-1} is given in [46] for neutron-irradiated n-type silicon with bulk doping concentrations (phosphorus) ranging from some 10^{11} cm^{-3} to some 10^{13}cm^{-3} (see also Fig. 10). The acceptor removal process after hadron irradiation has been less studied, but has become the field of high interest due to the recent shift from n-type to p-type silicon devices in the HEP community and the corresponding radiation damage effects [see Section III for p-type silicon sensors and Section VI for low-gain avalanche detectors (LGAD) and CMOS devices]. Some available data for the acceptor removal parameter c_A are shown in Fig. 10(b). As for the donor removal, a reciprocal dependence of the removal parameter on the initial acceptor concentration is found. While this dependence allows to perform radiation damage predictions (see [49] for an example of acceptor removal prediction on CMOS sensors), the underlying physics process of the dopant removal process remains difficult to be explained on the basis of defect kinetics of phosphorus, respectively boron, considerations alone [46], [54].

E. Charge Carrier Trapping

The charge carriers generated by ionizing particles or photons in the depleted bulk of the silicon sensor are traveling

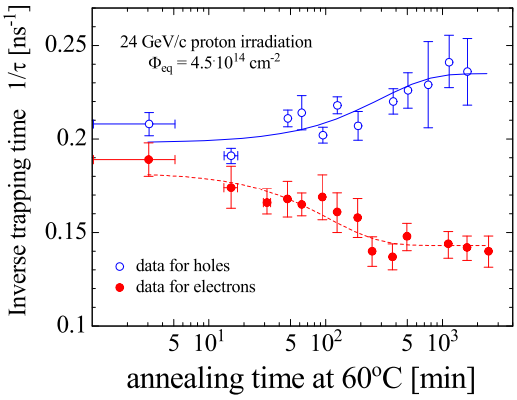

Fig. 12. Evolution of the inverse trapping time as function of annealing time at 60 °C. Data taken from [56].

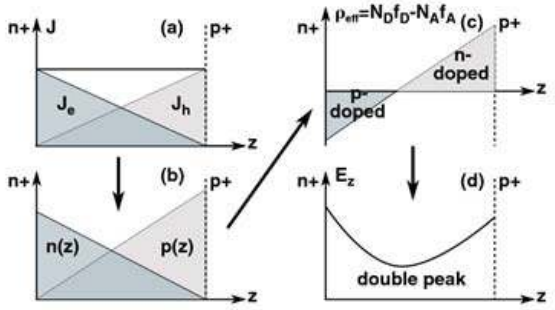

Fig. 13. Diagrams illustrate the polarization effect leading to a double-peak electric field distribution in sensor with high defect concentration. (a) Current density distribution due to the generation of leakage current. (b) Carrier density distribution with higher hole concentration due to lower hole mobility. (c) Distribution of space charge due to predominant trapping of electrons close to the n+ contact and holes close to the p+ contact. (d) Distribution of electric field strength arising out of space charge distribution given in (c) (see [40]).

toward the electrodes and constitute the sensor signal. If a charge carrier is trapped into a defect level and not released within the signal collection time of the sensor, the charge is lost and the corresponding sensor signal is reduced.

1) Fluence Dependence: With increasing defect concentration (increasing particle fluence), more and more charge carriers get trapped leading to a decrease of the charge collection efficiency (CCE), i.e., signal height of the sensor. The effective trapping time τ_{eff} can be used to describe this effect assuming that the loss of charge depends uniquely on the transport time of the charge carriers inside the sensor: $Q(t) = Q_0 \exp(-t/\tau_{\text{eff}})$. The effective trapping time can be separately measured for electrons and holes [56], [57]. As shown in Fig. 11, a linear dependence of the inverse effective trapping time on the particle fluence is observed and can be described as

$$1/\tau_{\text{eff}} = 1/\tau_{(\text{eff},0)} + \beta\phi_{\text{eq}} \tag{18}$$

where β is the proportionality factor (effective trapping damage constant) and $\tau_{\text{eff},0}$ is the effective carrier lifetime before irradiation, which in standard silicon already after very moderate radiation levels can be neglected. Similar values for various silicon materials (FZ [57], DOFZ [57], MCz [58], and EPI [59]) and different heavy particle irradiations [6], [57] have been observed, resulting in β values of 4–6 $\times$ 10^{-16} cm^2/ns for electrons and 5–8 $\times$ 10^{-16} cm^2/ns for holes. In a more recent work focusing on high-fluence irradiations, deviations from the linear behavior shown in Fig. 11 for particle fluences mentioned above about 3 $\times$ 10^{14} n_{eq}cm^{-2} were reported [60]. The inverse trapping time (trapping rate) increased slower than expected from the linear extrapolation from low-fluence data and gave, e.g., a 2–3 times lower value at 3 $\times$ 10^{15} n_{eq}cm^{-2}.

2) Annealing: As for the leakage current and the depletion voltage (effective doping concentration), the effective trapping damage constant depends on the annealing status of the sensor after irradiation. This is depicted in Fig. 12 for a proton irradiated sensor. While for electrons, a reduction in β_e (decrease in $1/\tau_{\text{eff},e}$, less trapping) with annealing time is observed, for holes (damage parameter β_h), an increase of trapping with time has been measured. The trapping damage constant β has been parameterized for electrons and holes as

$$\beta(t) = \beta_0 \exp(-t/\tau_a) + \beta_\infty(1 - \exp(-t/\tau_a)) \tag{19}$$

where β_0 and β_∞ denote the trapping rates β is at the beginning and end of the annealing process that is governed by the time constant τ_a [61].

3) Temperature Dependence: It has been shown that the trapping times are only weakly temperature dependent $\beta(T) = \beta(T_0)(T/T_0)^\kappa$ with κ in the range of -0.83–-0.90 for electrons [57], [58], [62] and -1.52–-1.69 for holes [57], [58].

F. Electric Field and Double Junction Effects

In the previous sections—and most importantly—in the transformation of the measured depletion voltage into effective space charge by 11, it is assumed that the space charge is homogeneously distributed over the sensor bulk and constant. The electric field is thus assumed to be a linear function of the depth in the sensor. However, in reality, this is not the case and all results on the effective space charge as deduced from, e.g., CV curves in form of depletion voltage characterization have to be treated with care. Only for nonirradiated sensors or low-irradiation fluences, the space charge can be assumed to be constant throughout the depleted sensor volume. For higher fluences, more complex field structures are observed. A fact which is most important for segmented detectors, as will be shown in Section III. Type inversion or SCSI in an n-type sensor (see Section II-C) was naively assumed to shift the space charge from positive to negative sign throughout the full sensor volume and consequently should lead to an electric field that starts to grow from the back electrode when rising the reverse bias over the sensor. While a strong electric field growing from the backside of the device is indeed observed, a field growing from the front side is also observed at the same time. The formation of such a double-peak field structure can be explained by a polarization effect [40] and is illustrated in Fig. 13. The free carriers (electrons and holes) generated by

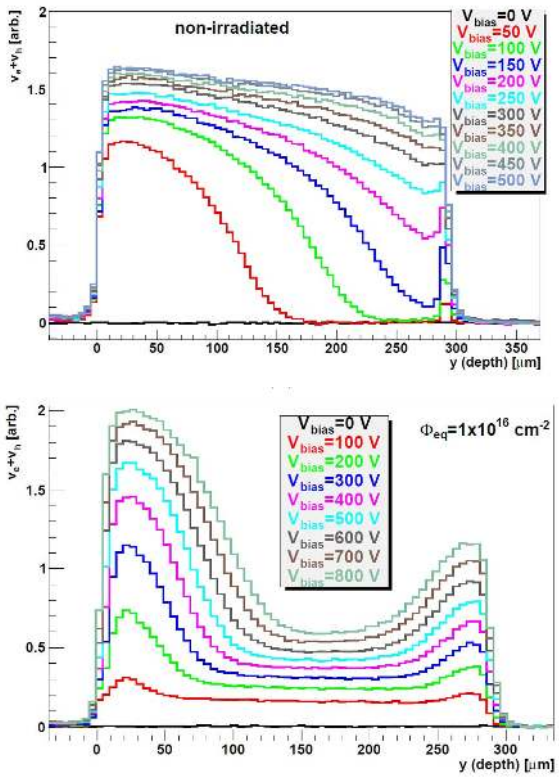

Fig. 14. Drift velocity profiles with varying bias voltages for a nonirradiated (top) and a neutron irradiated (10^{16} cm^{-2}) (bottom) p-type microstrip detector made from float zone silicon (5 kΩcm, 300 μm, and V_{dep} = 180 V). Figures taken from [66].

radiation-induced defects constitute the radiation-induced leakage current. As electrons are drifting toward the n+ electrode and holes toward the p+ electrode, the electron density is the highest at the n+ contact while the hole density is the highest at the p+ contact [see Fig. 13(b)]. The free carriers (electrons and holes) are partly trapped at radiation-induced defect levels (acceptors and donors), and thus build up additional space charge. This space charge is predominantly negative at the n+ contact and positive at the p+ contact [see Fig. 13(c)]. Finally, if the total effective space charge is negative at the n+ contact and positive at the p+ contact, a double-peak electric field distribution is observed [see Fig. 13(d)].

The transient current technique (TCT) allows to characterize and visualize the electric field distribution [63]–[65]. An example for a nonirradiated and highly irradiated sensor, as measured with edge-TCT is shown in Fig. 14 [66]. The depth profiles of the sum of the drift velocities of electrons (v_e) and holes (v_h) as created in the indicated depth of the sensor is shown. This parameter relates to the electric field strength E via $\vec{v}_e + \vec{v}_h = \mu_e(E)\vec{E} + \mu_h(E)\vec{E}$, where $\mu_{e,h}$ are the carrier mobilities. In cases where the drift velocity has not saturated as function of electric field strength, the sum of the drift velocities gives an image of the electric field strength within the sensor. It is clearly visible that the electric field in the nonirradiated sensor is growing from the front side while in the irradiated sensor fields are growing from both sides with rising reverse bias voltage.

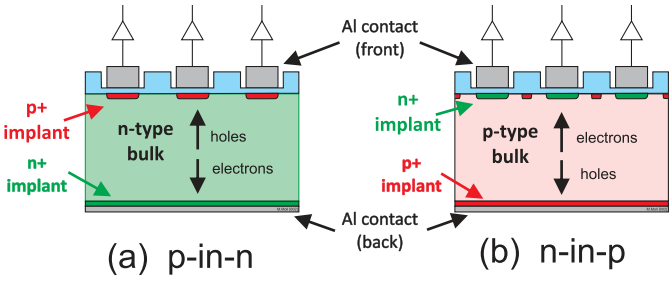

Fig. 15. Schematic of the (a) p-in-n and (b) n-in-p microstrip sensor concept. The p-in-n sensor consists of high-resistivity n-type bulk material with p-type implanted front electrodes (p+) and a homogeneous n-type implant (n+) on the backside. Negative potential is applied to the p+ implants with respect to the back contact. Holes are drifting to the top (front electrode) and electrons to the bottom (back electrode). For the n-in-p sensor the doping type is inverted and biasing is established by supplying positive potential to the front electrodes. In this case, electrons are drifting to the front electrode and holes to the back electrode. In both sensors, the strip electrodes are ac coupled via a thin oxide layer to the readout electronics while HV is applied via bias resistors directly to the front implants (not visible in figure).

While many measurements on the electric field distribution of irradiated sensors exist, a parameterization of the electric field distribution as function of silicon material, particle fluence and type, sensor thickness, temperature, and annealing time does not exist to the same comprehensive level as, e.g., for the effective space charge distribution presented in Section II-C. A proposal on how to parameterize the electric field distribution has been made [66], but needs to be completed with a bigger set of measured data. Another approach to predict the electric field distribution as function of the above-mentioned parameters is to use TCAD simulations. Here, the defect levels are parameterized and the electric field is calculated, offering the advantage that the parameterization becomes sensor geometry independent (see Section V).

III. Radiation Damage in Segmented Detectors

The results shown in Section II were obtained with pad detectors. These employ a single readout electrode with dimensions that are significantly larger than the thickness of the sensor (see Section II-A). In order to gain position information about the particle impact point, the detector has to be segmented into individual electrodes which are connected to individual readout electronics. The corresponding segmented sensors are called strip or pixel sensors according to the geometry of the segmentation. Strip sensors have a typical pitch (strip center-to-center distance) of 25–100 μm and a lengths range from centimeters to tens of centimeters. A schematic of strip sensors in a cut plane orthogonal to the strips is shown in Fig. 15. The pixel detectors are segmented along both dimensions (i.e., organized in a checkerboard pattern), and therefore, offer the best 2-D resolution. A more general introduction to segmented silicon sensors for particle tracking can be found in [9], [67], and [68]. Naturally, the basic radiation damage mechanisms in segmented and nonsegmented sensor configurations are identical. However, the fact that the electrodes are segmented impacts on the way the signal is formed on the electrodes which finally impacts on the detection efficiency and signal-to-noise ratio of the sensor.

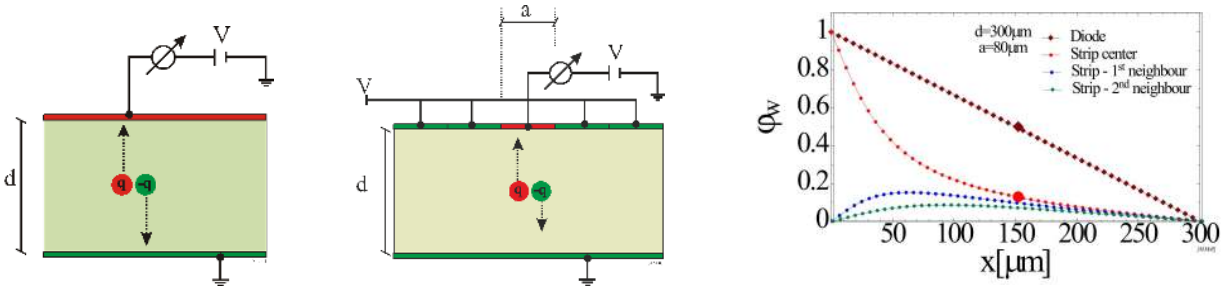

Fig. 16. Schematic of a diode (left), a strip (middle) sensor, and the corresponding weighting potentials (right) of the electrodes connected to the readout. Placing an electron-hole pair at the center of the sensor ($x = 150$ μm) would result in a 50%/50% contribution to the signal in case of the diode and a 87%/13% contribution of the hole/electron to the measured signal. The total collected charge is naturally the same for both types of detectors when the charge carriers have reached the electrodes.

In this section, we will first review the signal formation mechanism and then review radiation damage on segmented planar silicon sensors.

A. Signal Formation in Pad and Segmented Sensors

The instantaneous current I and the cumulated charge Q induced on the reading electrode of a sensor by a moving charge within the sensor volume can be calculated using the Shockley–Ramo theorem [69], [70]. It states that

$$I = q_0 \vec{v} \cdot \vec{E_W} = q_0 \mu(E) \vec{E} \cdot \vec{E_W} \quad \text{and} \quad Q = -q_0 \Delta \phi_W \tag{20}$$

where ϕ_W and $\vec{E_W}$ are the weighting potential and the weighting field of the electrode system and $\vec{v}$ is the velocity of the moving charge q_0, which can also be expressed as the product of mobility μ and electric field $\vec{E}$. The collected charge Q is given by the product of q_0 and the difference $\Delta\phi_W$ of the weighting potentials at the beginning and the end of the trajectory of the moving charge q_0. The weighting potential and field are calculated by removing all charges from the system-of-interest and setting all electrodes at zero potential with exception of the reading electrode that is set to unit potential. The difference in the weighting potential of a diode and a strip sensor is shown in Fig. 16. It is evident that in the parallel plate configuration at any position in depth (x-coordinate), the same amount of signal charge on the electrode is produced for a traversed Δx as the weighting field is a constant. This is completely different for segmented sensors, where charges traveling closer to the sensing electrode will produce a higher amount of signal charge for a traversed Δx than charges traveling further away from the electrode and traversing the same Δx. If not all generated charges will travel toward the collecting electrodes due to charge trapping by defects or underdepletion of the sensor volume, it is becoming very relevant for the sensor performance where the electric field is positioned (i.e., where the charges are drifting) and where it is not positioned. For radiation-damaged sensors which are impacted by trapping and underdepletion, it can be concluded as follows.

1) The type of carrier with the higher $\mu \cdot \tau_{\text{eff}}$ should be collected at the sensing electrode (electrons in the case of silicon).
2) The sensor shall be designed as such that the space charge distribution after irradiation is leading to the highest electric field being positioned at the sensing segmented electrode. This corresponds to the statement that the electric field E shall be high where the weighting field E_W is high (i.e., maximize $\vec{E} \cdot \vec{E_W}$). Underdepletion, if not avoidable, should occur in regions where E_W is small (i.e., usually the nonsegmented electrode on the backside of the sensor).

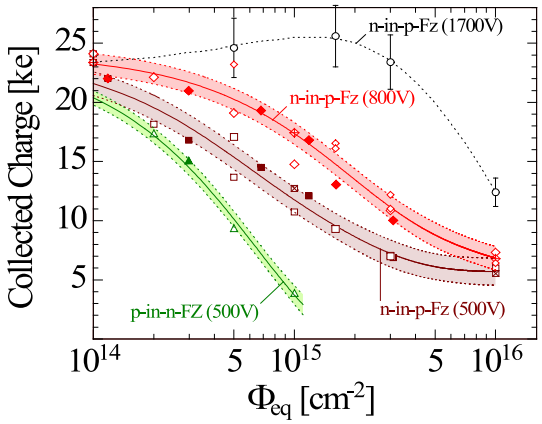

Fig. 17. Collected charge as function of n_{eq} fluence for 23-GeV proton, 26-MeV proton, and reactor neutron irradiated 300-μm-thick ministrip sensors. Measurements were taken at low temperatures (−20 °C to −40 °C) with the indicated bias voltages. Figure taken from [71].

These two recommendations represent fundamental support to the recent shift in strip sensor technology for the next generation main HL-LHC tracking detectors from the p-in-n sensors toward n-in-p sensors (see Fig. 15 and Section III-B). It shall be emphasized that this shift is not driven by the conduction type of the bulk material (i.e., n-type or p-type), but by the fact that the sensing electrode in p-type bulk sensors is the electrode connected to the n+ implant, which is collecting electrons and which happens to be closer to the region of the highest electric field after heavy irradiation for the standard silicon materials.

B. Segmented Sensors With n-Electrode Readout (n-in-p and n-in-n Sensors)

Current ATLAS and CMS strip tracking detectors at the LHC are based on the p-in-n concept while the future detectors at the HL-LHC will be based on the n-in-p concept. Fig. 17 shows a collection of various results obtained within

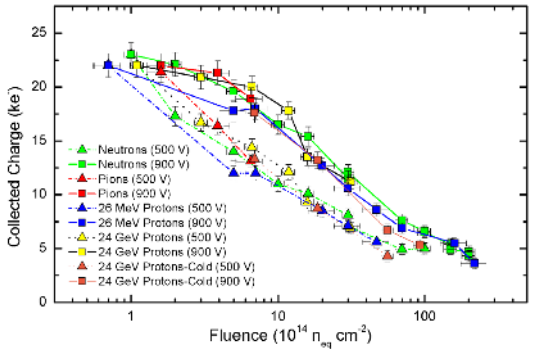

Fig. 18. ATLAS: collected cluster charge in 300-μm-thick n-in-p FZ silicon sensors for various particle types and two applied voltages, 500 and 900 V. Figure taken from [73].

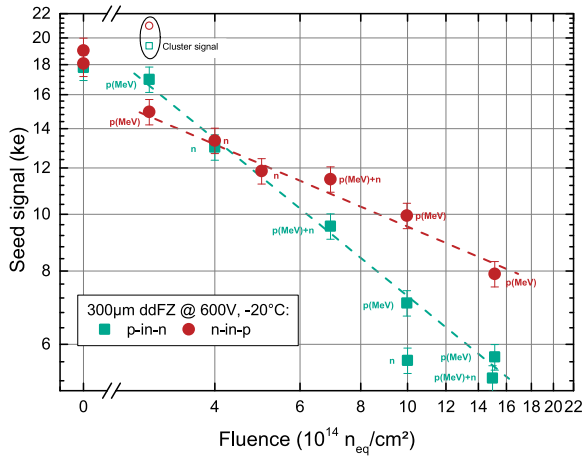

Fig. 19. CMS: charge collected on the seed strip (strip with the highest signal in a cluster) versus fluence for 600 V biasing at −20 °C after short annealing (2–6 days) at room temperature, for sensors with nominal thicknesses of 300 μm. The text next to the symbols indicates the irradiation particle type (p stands for protons in the MeV energy range and n for reactor neutrons). Lines are drawn to guide the eye. Figure reproduced from [74].

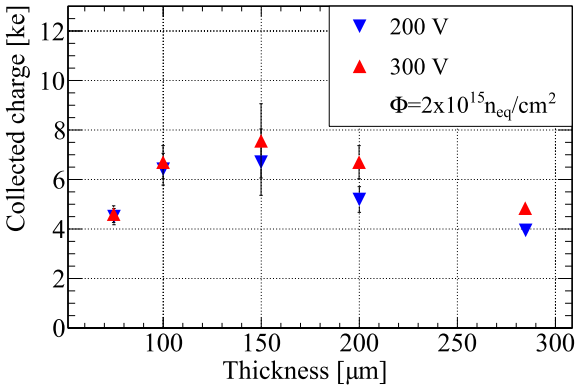

Fig. 20. Charge collection of n-in-p pixel sensors as function of the thickness of the sensor. Measurements were taken after irradiation with 2×10^{15} n_{eq}cm^{-2} at voltages of 200 and 300 V and a temperature of −40 °C. Figure taken from [76].

the RD50 collaboration on n-in-p sensors and demonstrates the motivation for going from p-electrode (here: p-in-n) toward n-electrode (here: n-in-p) readout. After irradiation with a fluence of 10^{15} n_{eq}cm^{-2}, the p-type sensors can still provide

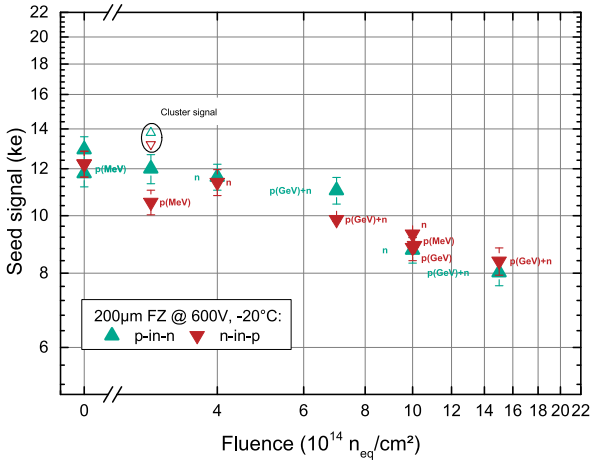

Fig. 21. Charge collected on the seed strip (strip with the highest signal in a cluster) versus fluence for 600 V biasing at −20 °C after short annealing (0 to 50 days) at room temperature, for sensor thicknesses of 200 μm. The text next to the symbols indicates the irradiation particle type (p stands for protons in the MeV/GeV energy range and n for reactor neutrons). Figure reproduced from [74].

a signal of about 10 000 electrons with an applied voltage of 500 V. The signal can still be increased applying higher voltages. When going toward extreme voltages, such as 1700 V shown in Fig. 17, impact ionization in the high-field regions inside the sensor will lead to signals that are corresponding to the signal of nonirradiated sensors or even higher. Following the successful demonstration of the improved radiation hardness of the n-in-p technology, the ATLAS and CMS tracker collaborations conducted further comprehensive research and development campaigns on n-in-p sensors, focusing on radiation hardness studies tailored to their specific radiation environments but also on technology challenges such as the interstrip isolation in p-type sensors, reduction of dead area at the sensor edges, mass production, and overall performance optimization. Results produced by the ATLAS [72], [73] and CMS [16], [74] tracker collaborations on 300-μm-thick sensors are shown in Figs. 18 and 19 and fully support the earlier results of the RD50 collaboration.

C. Segmented n-in-p Sensors—Signal Dependence on Sensor Thickness

The results presented in the previous sections focused on 300-μm-thick sensors. Studies on thinner sensors revealed a strong dependence of the signal on the sensor thickness. It was, for example, found that 140-μm-thick n-in-p strip sensors deliver a bigger signal than 300-μm-thick sensors when irradiated to beyond about 10^{15} n_{eq}/cm^2 [75]. The same holds for n-in-p pixel sensors as demonstrated in Fig. 20 [76]. The plot demonstrates that (depending on the particle fluence and the applied voltage) an optimum thickness of the device can be found to maximize the measured signal. The reason for this complex dependence on particle fluence, device thickness, electrode geometry, and operation temperature is found in the strong charge trapping (see Section II-E), the weighting field geometry of the sensors (see Section III-A), and the

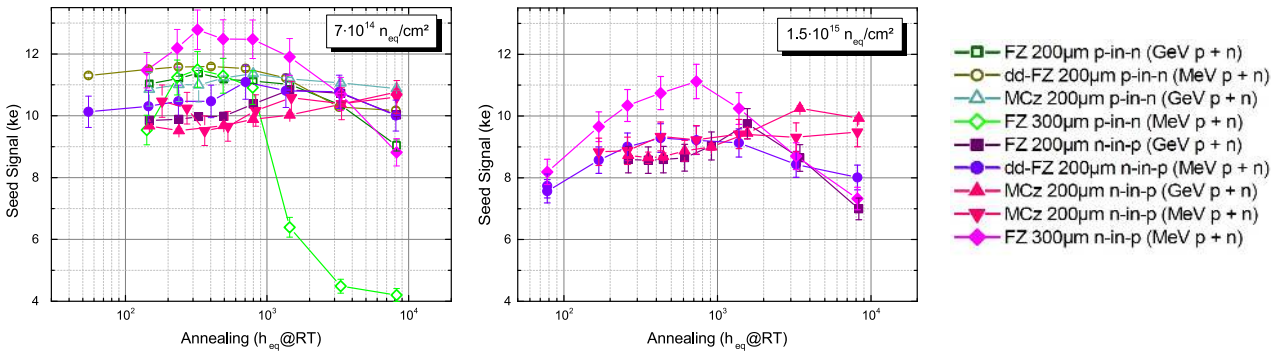

Fig. 22. Charge collected on the seed strip (strip with the highest signal in a cluster) versus room temperature equivalent annealing time for two different fluences. Measurements were taken with 600 V at −20 °C. The sensor thickness, the material type, and the particle mix used for irradiation are indicated in the legend (FZ: floating zone, dd-FZ: deep diffused FZ, and MCz: magnetic Czochralski). Figure reproduced from [16].

complex electric field structure after irradiation (see Section II-F). The CMS collaboration demonstrated furthermore that the advantage in using n-in-p strip sensors instead of p-in-n sensors is not clearly evidenced for 200-μm-thick sensors (see Fig. 21) compared to the case of 300-μm-thick sensors (see Fig. 19) [16]. The degradation in terms of signal charge versus fluence seems to follow a very similar behavior. However, p-in-n sensors were nevertheless abandoned as they showed nonGaussian noise contributions after high-radiation levels, resulting in an irreducible rate of fake hits that would in some cases be as large as the expected signal occupancy [74]. Device simulations have shown that irradiated p-in-n strip sensors develop high electric fields at the strip edges that intensify with increasing accumulation of oxide charge. The electric fields around the strips in n-in-p sensors are instead reduced by higher oxide charge, which makes them more robust with respect to effects such as breakdown, noise, or microdischarge after heavy irradiation with charged particles [16].

D. Annealing of Segmented Planar n-in-p Sensors

A further striking feature of 300-μm-thick n-in-p strip sensors is that—contrary to p-in-n sensors of same thickness—the collected charge for highly irradiated detectors is less dramatically influenced by the reverse annealing of the effective space charge [16], [77], [78]. This is, for example, shown in Fig. 22(left) where the signal for the p-in-n sensor dramatically drops with annealing time, while the p-type sensor shows much lower changes. Even more interesting are the results for thin sensors: no significant degradation of the signal has been observed for the 200-μm-thin strip sensors after long-term annealing (see Fig. 22). Thus, a promising detector concept has been found that after exposure to irradiation does not suffer, but rather benefits from periods at elevated temperatures: the leakage current is annealing (getting smaller), while the collected signal charge remains constant.

E. 3-D Sensors

The 3-D silicon detector technology was proposed in 1997 [79] and consists of columnar electrodes etched perpendicularly to the wafer surface as schematically shown

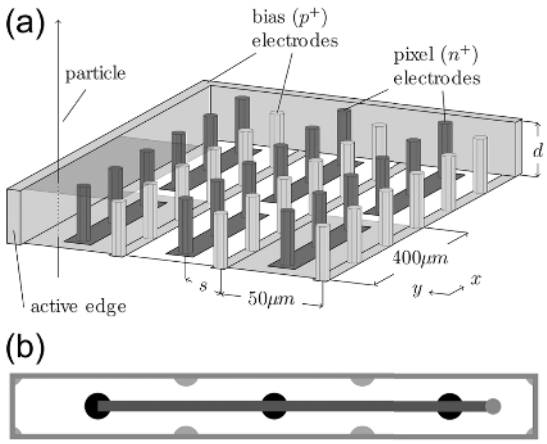

Fig. 23. (a) Schematic of 3-D silicon structures (x and y dimensions are not to scale) with p and n electrodes and an active edge, $s = 70$ μm and $d = 210$ μm. (b) View from the top of one pixel cell showing the n and p electrodes and the metallization connecting electrodes of the same type. Figure taken from [80].

in Fig. 23. This geometry decouples the active thickness of the device, i.e., the length penetrated by the ionizing particle, from the charge carrier drift length, i.e., the distance the charges have to travel to the electrodes. The small distance between the columns (about 50–100 μm) translates into small depletion voltage and fast charge collection, and is thus an intrinsically more radiation hard device concept than corresponding planar 300-μm-thick devices. Less charge get trapped in heavily irradiated devices due to the shorter drift distance to the electrodes, and since the device can be operated with lower voltages, the power consumption is drastically reduced. Disadvantages of 3-D in comparison to planar pixel sensors are the higher pixel capacitance leading to higher noise, a dead region around the columns, and larger production costs. Fig. 23 shows the configuration of a pixel cell by connecting three n+ columns for a readout electrode matching the pixel size of 50 μm × 400 μm of the ATLAS FE-I3 pixel readout chip [80]. Naturally, strip sensors and large size diodes can also be fabricated in 3-D technology by interconnecting the columns accordingly.

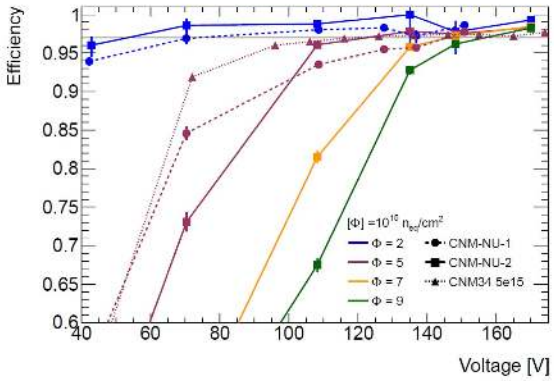

Fig. 24. Hit efficiency versus voltage for different fluences up to 9×10^{15} $n_{\mathrm{eq}}\mathrm{cm}^{-2}$. The 97% benchmark efficiency aimed for is marked. Figure taken from [81].

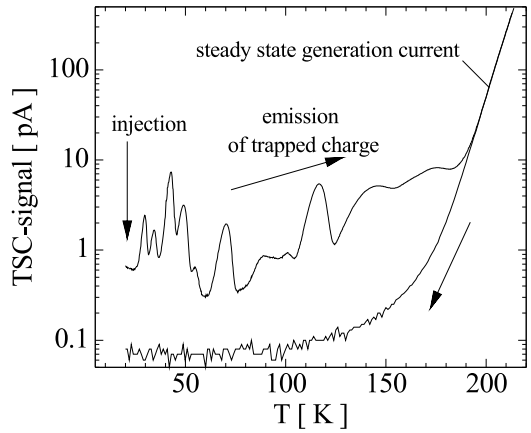

Fig. 25. Typical TSC spectrum measured on an FZ sensor irradiated with neutrons ($\phi_{\mathrm{eq}} = 1 \times 10^{13}$ $n_{\mathrm{eq}}/\mathrm{cm}^2$). Measured after 100-min annealing at RT. Injection by forward biasing (30 s, 6.8 mA/cm^2) at 20 K. Temperature ramping up with 0.183 K/s under 100 V reverse bias on the 300-μm-thick sensor. Figure taken from [35].

The production challenges of 3-D sensors have been overcome [82], [83] and their good performance lead to the recent installation of 3-D sensors in the innermost pixel layer of the ATLAS experiment, the so-called ATLAS b-layer [84]. Fig. 24 gives an example of the excellent performance of 3-D silicon sensors after very high irradiation levels [81]. Even after 9×10^{15} $n_{\mathrm{eq}}/\mathrm{cm}^2$, a hit efficiency in a test beam with normal beam incidence of more than 97% is reached below 200 V. In conclusion, it can be stated that 3-D sensors are excellent sensor candidates for the HL-LHC upgrade of the ATLAS and CMS pixel detectors.

IV. Radiation-Induced Defects With an Impact on Sensor Performance

The characterization and identification of the radiation-induced defects responsible for the deterioration of the various device properties is of crucial importance for the understanding, simulation, and mitigation of radiation damage effects. In this section, we give a short review of characterization methods, identified defects, and examples where the macroscopic degradation of the electrical properties of the sensors has been unambiguously linked to specific defects.

A. Defect Characterization Methods

There are various characterization methods that measure different properties of the defects and are sensitive to different defect concentrations (see [85] for techniques dedicated to highly damaged silicon sensors). Of the highest interest for understanding the impact of defects on the performance is the electrical characterization of the defects gaining parameters such as the capture cross sections, level position in the band gap and concentration (see Section I-D), as well as their thermal stability (annealing behavior) through the long-term or elevated temperature annealing studies. Here, capacitance–deep level transient spectroscopy (C-DLTS) [86] is the most sensitive and also the most common method, which however, has a strong limitation in the requirement that the concentration of defects has to be smaller than the shallow doping of the device. As sensors are made from high-resistivity material (low-doping concentration) and are exposed to severe radiation levels (defect concentration surpassing doping concentration by several orders of magnitude), other methods are needed to extend the range of defect spectroscopy toward higher damage levels (particle fluence ranges). The thermally stimulated current's (TSCs) method has been proven to be a very useful tool that led to the discovery and characterization of several defect levels causing radiation damage and observed at higher particle fluences. An example of a measurement is shown in Fig. 25 and based on the following working principles.

1) *Cooling* of the sample to low temperatures (with or without biasing).
2) *Charge injection:* filling of the traps by illumination or by forward biasing.
3) *Measurement of spectrum:* Heating the sample under reverse bias with a constant heating rate and monitoring the discharging current due to thermal emission from the defect levels.

To determine the structure and chemical composition of the defects further methods are needed. The atomic structure of paramagnetic defects can be studied by electron parametric resonance [85], [87], and modern electron microscopes allow to perform a high-resolution transmission electron spectroscopy resolving the crystal structure down to the atomic level [85]. Optical methods like Fourier-transform infrared spectroscopy (FTIR) allow identifying the defects via their characteristic vibration modes (frequencies) and estimate their concentration from the overall absorption. The full identification of a defect with its structural and electrical properties requires extensive correlation studies employing various techniques on the same material or device and is a very working intensive procedure. A summary with some successful examples with relevance for the performance degradation of highly damaged silicon devices will be given in the next section.

B. Point and Cluster Defects

In this section, we briefly review some of the most important defects with an impact on the macroscopic detector performance without being able to give a comprehensive overview.

TABLE I

ELECTRICAL PROPERTIES OF POINT AND EXTENDED DEFECTS RELEVANT FOR DETECTOR OPERATION (SEE [32] AND REFERENCES GIVEN IN THE TABLE)

Defect	Transition	Level(s) [eV]	$\sigma_{e,h}$ [cm^2]	Comment
E(30K)	(0/+)	$E_C - 0.1$	$\sigma_e = 2.3 \times 10^{-14}$	Not identified extended defect, donor level, contributes in full concentration with positive space charge to N_{eff}, strongly generated after charged particle irradiation with linear fluence dependence [32], [37], [89].
BD_A	(0/++)	$E_C - 0.225$	$\sigma_e = 2.3 \times 10^{-14}$	Point defect, TDD2, bistable donor existing in configuration A and B, strongly generated in O rich material, contributing in full concentration to positive space charge [36], [90], [91]
BD_B	(+/++)	$E_C - 0.15$	$\sigma_e = 2.7 \times 10^{-12}$	
I_p	(+/0)	$E_V + 0.23$	$\sigma_h = (0.5 - 9) \times 10^{-15}$	Not identified point defect, tentatively V_2O or C related defect [37], generated via second order process (quadratic fluence dependence), strongly generated in O lean material, acceptor level contributing to current and N_{eff} [36], [37], [92], [93]
	(0/-)	$E_C - 0.545$	$\sigma_e = 1.7 \times 10^{-15}$ $\sigma_h = 9 \times 10^{-14}$	
E_{75}	(-/0)	$E_C - 0.075$	$\sigma_e = 3.7 \times 10^{-15}$	Tri-Vacancy (V_3), bistable defect existing in 2 configurations: FFC(E_{75}) and PHR(E4,E5), E5 is contributing to leakage current, linear fluence dependence [37], [94]–[98]
E4	(=/-)	$E_C - 0.359$	$\sigma_e = 2.15 \times 10^{-15}$	
E5	(-/0)	$E_C - 0.458$	$\sigma_e = 2.4 \times 10^{-15}$ $\sigma_h = 2.15 \times 10^{-13}$	
H(116K)	(0/-)	$E_V + 0.33$	$\sigma_h = 4 \times 10^{-14}$	3 non identified extended defects, linear fluence dependence, contributing in full cocentration negative space charge, responsible for *reverse annealing* [32], [37], [89], [99]
H(140K)	(0/-)	$E_V + 036$	$\sigma_h = 2.5 \times 10^{-15}$	
H(152K)	(0/-)	$E_V + 0.42$	$\sigma_h = 2.3 \times 10^{-14}$	
BiOi	(0/+)	$E_C - 0.23$		Dominant Boron related defect (electron trap) in oxygen rich Silicon, created during acceptor removal [100]–[103]

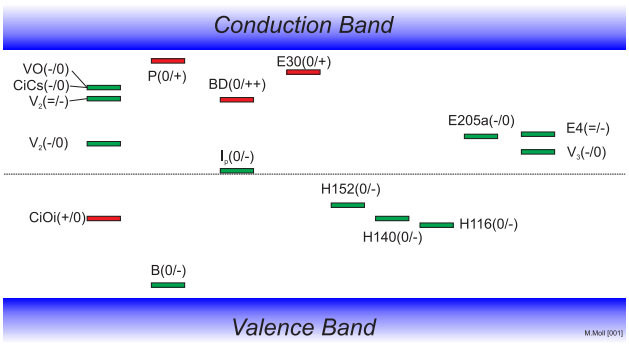

Fig. 26. Schematic of a selection of defect levels generated by radiation in the silicon band gap. Red: donors and Green: acceptors. Note that within the SCR of depleted diodes acceptors in the lower half of the band gap provide negative space charge and donors in the upper half of the band gap positive space charge. Details about the levels are given in the text and in Table I.

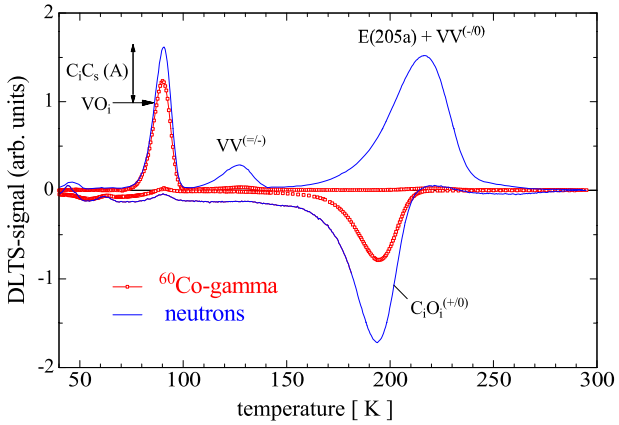

Fig. 27. DLTS spectra for neutron and ^{60}Co-gamma irradiated identical high resistivity FZ devices. The spectra are scaled to the signal of the vacancy-oxygen level VO_i which is overlapping with the C_iC_s level [35], [104].

For a more detailed review, the reader is addressed to refer [32], [37], and [88] and literature cited therein.

Table I and Fig. 26 give an overview of the most relevant defects, their properties and their impact on detector operation. The relation between the basic defect parameters (electron and hole cross sections, position in the bandgap, charge states, and concentration) and the macroscopic detector properties (space charge, generation current, and trapping) was already discussed in Section I-D. We furthermore distinguish between point defects and extended defects (or cluster defects). Irradiation with ^{60}Co-gammas or low-energy electrons up to some MeV can only lead to single atom displacements, and thus to the creation of point defects only. Irradiation with neutrons leads predominantly to defect clusters and a few point defects. High-energetic charged particles, such as protons, lead to a mix of point and cluster defects (see Section I-C and Fig. 4). Experimentally, a comparison of gamma- and neutron-irradiated sensors helps to determine the classification into point and cluster defects (see Fig. 27 and [104]). Another approach is to irradiate identical devices with electrons of increasing energy scanning over the threshold recoil energy for cluster formation as shown in Fig. 28 [105]. Obviously, the assignment into point defects and cluster defects is not strict. The V2 (the divacancy), for example, is *per se* a point defect while it is also found after neutron irradiation inside defect clusters where lattice strain is leading to a distortion of its properties in terms of the width of its energy level distribution and charge carrier capture behavior [106], [107].

V. DEVICE SIMULATIONS

Device simulations have become an integral part of any detector development project. They allow understanding, testing, and optimizing devices in the design phase before they even have been built. Also simulations of radiation-damaged

TABLE II

COLLECTION (NONEXHAUSTIVE) OF RADIATION DAMAGE MODELS USED TO SIMULATE THE ELECTRIC FIELD WITHIN SILICON SENSORS AFTER HIGH FLUENCE HEAVY PARTICLE IRRADIATION (SEE TEXT). A: ACCEPTOR AND D: DONOR

Model	Type	Level [eV]	$\sigma_{e,h}$ [cm^2]	η [cm^{-1}]	Comment
EVL 2002 [40]	A	$E_C - 0.525$	1×10^{-15}	–	Tool: Microsoft Excel [116]
	D	$E_V + 0.48$	1×10^{-15}	–	
	–	$E_C - 0.65^{(*)}$	1×10^{-13}	0.4	$^{(*)}$level for current generation, no space charge
Perugia 2006 [109]	A	$E_C - 0.42$	$2 \times 10^{-15}, 2 \times 10^{-14}$	1.613	Tool: Silvaco [117]
(p-type sensors)	A	$E_C - 0.46$	$5 \times 10^{-15}, 5 \times 10^{-14}$	0.9	
	D	$E_V + 0.36$	$2.5 \times 10^{-14}, 2.5 \times 10^{-15}$	0.9	
	A	$E_C - 0.42$	$2 \times 10^{-15}, 1.2 \times 10^{-14}$	13	
(n-type sensors)	A	$E_C - 0.50$	$5 \times 10^{-15}, 3.5 \times 10^{-14}$	0.08	
	D	$E_V + 0.36$	$2 \times 10^{-18}, 2.5 \times 10^{-15}$	1.1	
Glasgow 2008 [110]	A	$E_C - 0.42$	$9.5 \times 10^{-15}, 9.5 \times 10^{-14}$	1.613	Tool: Synopsys [118]
	A	$E_C - 0.46$	$5 \times 10^{-15}, 5 \times 10^{-14}$	0.9	model adapted from *Perugia 2006* [109]
	D	$E_V + 0.36$	$3.23 \times 10^{-13}, 3.23 \times 10^{-14}$	0.9	simulation of p-type 3D sensors
KIT 2013 [111]					Tool: Synopsys [118]
(protons)	A	$E_C - 0.525$	$1 \times 10^{-14}, 1 \times 10^{-14}$	–	$\eta_A = 1.189\ \text{cm}^{-1} \times \phi - 6.454 \times 10^{13}\ \text{cm}^{-3}$
	D	$E_V + 0.48$	$1 \times 10^{-14}, 1 \times 10^{-14}$	–	$\eta_D = 5.598\ \text{cm}^{-1} \times \phi - 3.949 \times 10^{14}\ \text{cm}^{-3}$
(neutrons)	A	$E_C - 0.525$	$1.2 \times 10^{-14}, 1.2 \times 10^{-14}$	1.55	
	D	$E_V + 0.48$	$1.2 \times 10^{-14}, 1.2 \times 10^{-14}$	1.395	
Delhi 2014 [112]	A	$E_C - 0.51$	$2 \times 10^{-14}, 2.6 \times 10^{-14}$	4	Tool: Silvaco [117]
	D	$E_V + 0.48$	2×10^{-14}	3	
Perugia 2016 [113]	A	$E_C - 0.42$	$1 \times 10^{-15}, 1 \times 10^{-14}$	1.613	improving *Perugia 2006* [109]
(p-type sensors)	A	$E_C - 0.46$	$7 \times 10^{-15}, 7 \times 10^{-14}$	0.9	$\phi_{eq} \leq 7 \times 10^{15}\ \text{cm}^{-2}$
	–	–	$3 \times 10^{-15}, 3 \times 10^{-14}$	–	$7 \times 10^{15}\ \text{cm}^{-2} \leq \phi_{eq} \leq 1.5 \times 10^{16}\ \text{cm}^{-2}$
	–	–	$1.5 \times 10^{-15}, 1.5 \times 10^{-14}$	–	$1.5 \times 10^{16}\ \text{cm}^{-2} \leq \phi_{eq} \leq 2.2 \times 10^{16}\ \text{cm}^{-2}$
	D	$E_V + 0.36$	$3.23 \times 10^{-13}, 3.23 \times 10^{-14}$	0.9	

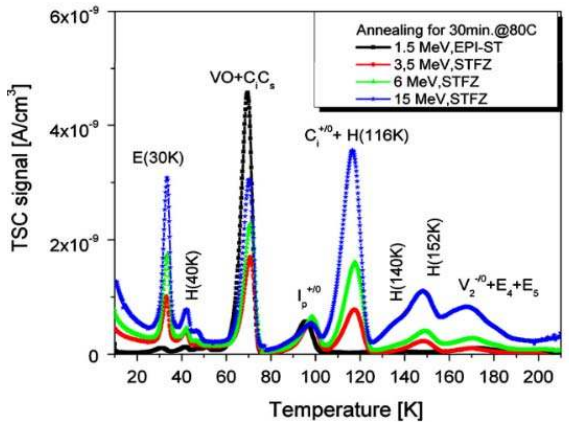

Fig. 28. TSC spectra for different electron energies measured for 1.5-MeV electrons on standard epitaxial silicon (EPI-ST) and for 3.5-, 6-, and 15-MeV electrons on standard floating zone silicon.

devices using TCAD programs have made enormous progress over recent years (see [108]). The increasing knowledge on the radiation-induced defects (see Section IV) allows implementing realistic defect levels into the simulators. However, the significant number of defect levels observed after irradiation increases the complexity of the numerical simulation. The large set of defects needs to be reduced to a small number of effective defect levels to allow for calculations to converge. The outcome of simulations with these effective defect levels is then benchmarked and optimized against measured macroscopic detector parameters until the optimization procedure results into a good agreement with a larger data set. Having gained confidence in the parameter sets, these are then used to predict the radiation-induced degradation of sensors with different geometries or operation conditions. Several models (defect parameter sets) have been published employing a varying number of defect levels [40], [109]–[113]. A nonexhaustive list of models is given in Table II. Some models also integrate the handling of radiation-induced surface damage in the dielectric layers and at the interface between the dielectric and the silicon bulk [113]–[115]. The optimization of the defect parameter set used in TCAD simulations is usually performed manually due to the complexity and the corresponding time consumption of the simulations. In a recent approach [119], the optimizer of the Synopsys Sentaurus TCAD package was used to fit measurement data, i.e., minimize the difference between simulation and measurements, by varying the defect parameters. A set of capacitance–voltage (CV) and current–voltage (IV) measurements on highly irradiated diodes was used to obtain a set of defect parameters (two defect levels, i.e., eight free parameters) that then was used to simulate a CCE measurement with an infrared laser. Simulations performed with parameter sets from literature were added for comparison (see Table II). The investigation demonstrates that the presently available TCAD defect parameter sets lead to significantly different results when applied to highly irradiated silicon diodes. The approach to fit multiple measurement data in parallel seems to be very fruitful, but also demonstrates that two effective defect levels are not sufficient to fully describe the experimental data. In conclusion, it can be stated that

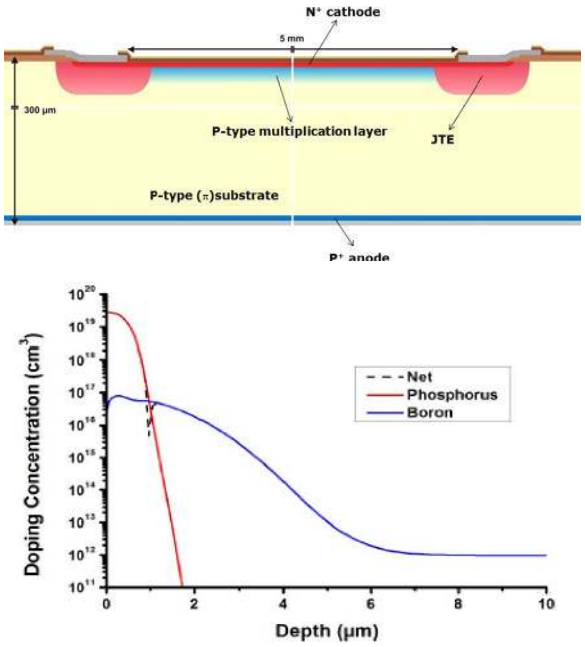

Fig. 29. Schematic cross section of the LGAD design with a JTE structure protecting the JTE (top). Simulated doping profile at the n++−p+ junction in the center of the device (bottom). Figures taken from [120].

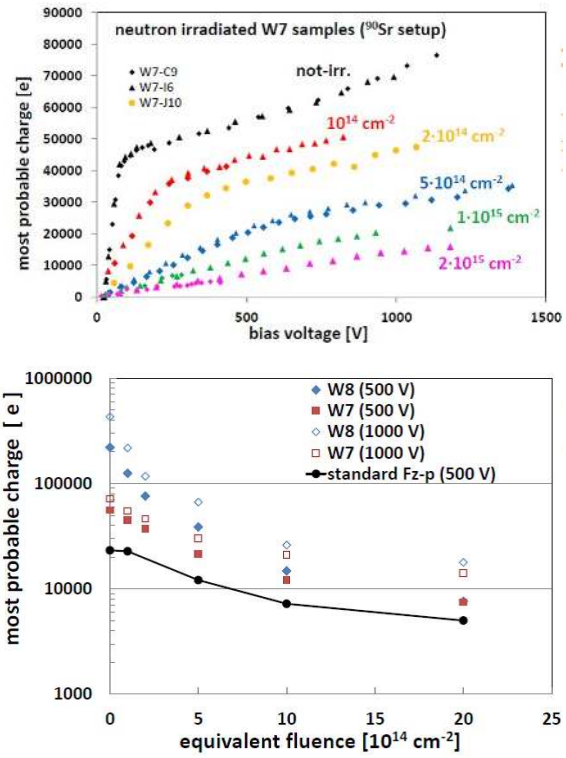

Fig. 30. Dependence of most probable charge of LGAD sensors on voltage at different neutron fluences (W7) (top). Dependence of measured charge on equivalent neutron fluence at 500 and 1000 V (bottom). Figures taken from [123].

the method of using TCAD simulations with effective defect level parameters is a very powerful tool to understand and predict radiation damage to silicon devices. They have helped to optimize many sensors with respect to radiation hardness, while care has to be taken that not all experimental effects can be explained. Further work is needed to increase the accuracy of these simulations.

VI. Devices

A. Low Gain Avalanche Detectors

Avalanche detectors are devices exploiting the avalanche multiplication in the high-field regions to enhance the signal produced by a photon or a particle in the bulk of the device. The avalanche photo diode (APD) is the most prominent with high-signal gain and a wide application field. More recently, LGADs have been developed with the aim to improve timing and particle detection performance in HEP experiments [120]–[122]. Compared to standard reach-through APDs, they have a lower gain in the order of 10 allowing for a stable operation with a linear amplification of the signal over a wide voltage range. Fig. 29 depicts the schematic of an LGAD device and a simulated typical doping profile of the upper side of the sensor. The high electric field ($>2 \times 10^5$ V/cm) in the p-type multiplication layer (p+) leads to avalanche multiplication of electrons traversing the layer, and thus, to a gain in the signal with respect to an identical sensor without the multiplication layer. In order to prevent premature breakdown of the device, the p+ multiplication layer has to be properly terminated, which is realized for the LGAD devices by a deep n-type diffusion surrounding the p+ multiplication layer. This structure is called junction termination extension (JTE).

Irradiation of the devices with heavy particles leads to the expected increase of leakage current (see Section II-B), and consequently to a significant increase in sensor noise as the thermally generated charge carriers are undergoing charge multiplication in the same way as the charge carriers produced by the impinging particle or photon are multiplied. The multiplication is even stronger for the thermally generated carriers than for the carriers composing the signal, as the latter are suffering from charge trapping (see Section II-E), while the leakage current is a steady-state effect [123]. Based on this fact, the advantage of the increased signal of the LGAD device is expected to give an advantage over conventional detectors for small cell volumes and fast shaping times [123] and in particular for complex detector systems such as pixel sensors with other significant noise sources. Also, the multiplication layer in LGAD is impacted by a displacement damage leading to a significant degradation in the gain with increasing fast hadron fluence reaching a complete loss of gain at a fast-charged particle fluence of about 5×10^{14} cm^{-2} and leaving only little gain after exposure to neutron fluences of 2×10^{15} cm^{-2} [123], [124].

Fig. 30 shows a series of the most probable charge collected by LGAD sensors exposed to electrons of a ^{90}Sr source after irradiation with neutrons to different fluences. The signal degradation is clearly visible and compared in Fig. 30 (bottom) to a standard n-in-p sensor without intrinsic gain. The gain decrease is attributed to the reduction of effective doping concentration in the multiplication layer,

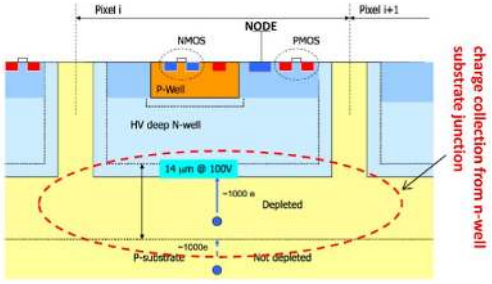

Fig. 31. Schematic of an HV-CMOS detector cross section. The region-of-interest, where the depletion region grows with growing applied bias, is indicated. Figure taken from [49].

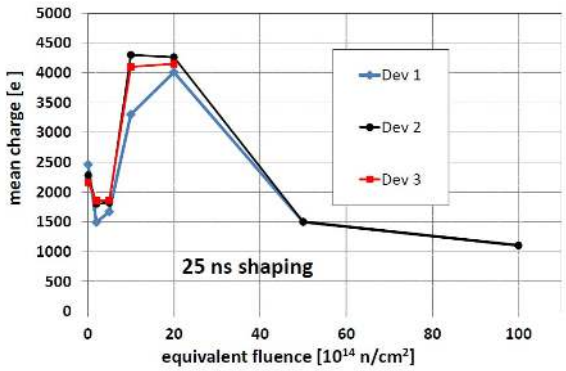

Fig. 32. Mean charge at 120 V versus fluence for different devices (350-nm technology). The measurements shown at 5×10^{15} cm^{-2} were taken at 100 V. The lines are used to guide the eye. Figure taken from [49].

which leads to smaller electric field strengths, and thus a reduction in gain [123]. The origin has been attributed to the deactivation of boron acceptors in the amplification layer [123], to a compensation mechanisms by charged defects without boron deactivation [125] or to a combination of charged defects, moderate boron deactivation, and a strong hole trapping [126] (see Section II-D).

B. HV-CMOS

The HV-CMOS process allows to apply high-bias voltages to the substrate of CMOS sensors and collect charges from deep n-wells in a p-type substrate [127]. Several different sensor designs exist (see [128] for a recent review) and a schematic cross section of a pixelated device is shown in Fig. 31. All transistors are placed in a lowly doped-deep n-well. The PMOS transistors are placed directly in the n-well, while the NMOS transistors are in the seperate p-wells. The deep n-well is biased with HV (typically more than 50 V) with respect to the substrate. The depletion depth of the substrate, and thus the signal heights for particle detection depends on the resistivity of the substrate. Radiation damage tests have shown that the depletion depth changes significantly due to displacement damage effects [49]. An example of the dependence of the collected charge on particle fluence is shown in Fig. 32 for sensors produced in a 350-nm technology on a 20-Ωcm substrate. For low fluences, the collected charge first decreases due to the increase of charge trapping that is reducing the contribution of diffusing charges. However, from about 10^{15} cm^{-2}, the signal rises due to the decrease of substrate resistivity, and consequently an increase in depletion depth. The reason is mainly found in the radiation-induced acceptor removal (see Section II-D). The signal doubles at $1–2\times10^{15}$ cm^{-2} with respect to the value obtained before irradiation. Finally, above about 2×10^{15} cm^{-2}, the signal decreases again due to the increase of deep acceptors (see Section II-C) and the increasing probability to also trap the drifting charge carriers in defect levels (see Section II-E).

VII. Radiation Damage in Tracking Detector Silicon Sensors Operating in the LHC

The LHC tracking detectors are operating in harsh radiation environments (see Section I-A) and are thus suffering from radiation damage effects [129]. The detrimental effects of

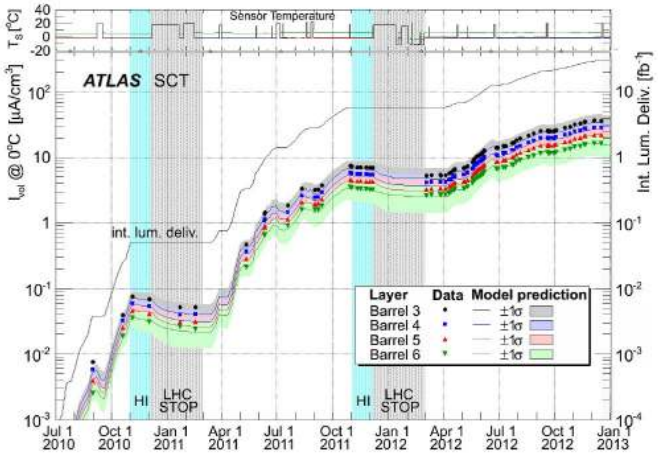

Fig. 33. Comparison between data (points) and model predictions (lines with uncertainties shown by the colored bands) of the leakage current per unit volume at 0 °C (Ivol) of the four barrel layers. The integrated luminosity and the average sensor temperatures are also shown. The blue shading and label HI indicate periods of heavy-ion running, while extended periods with no beam in the LHC during which the SCT was OFF are shaded gray. Figure taken from [132].

radiation on the tracking detectors include: 1) increasing leakage currents; 2) charge accumulation in silicon oxide layers; 3) single-event upsets; 4) decreasing signal-to-noise ratio; 5) changing depletion voltages; and 6) radiation-induced activation of components. Typically, both sensors and readout electronics are affected, but in the case of single-event upsets only the readout system is impacted. The radiation fields have been simulated with advanced Monte Carlo event generators and particle transport codes and were translated into maps of 1-MeV neutron equivalent fluences (n_{eq}) employing the NIEL hypothesis. Radiation damage models [35], [130]–[132] are then employed using the available information on the instantaneous luminosity and device temperature as a function of time to compare the observed degradation with previous experiments and predict the radiation damage for the future years. An example for the increase of sensor leakage current in the ATLAS silicon central tracker is shown in Fig. 33 [132]. The measurements of the increase in leakage currents with time are consistent with the radiation damage predictions.

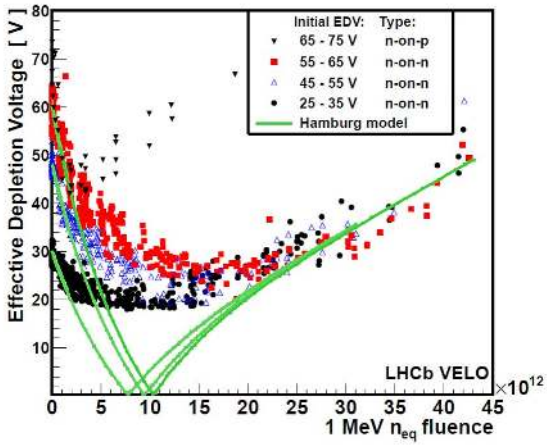

Fig. 34. Effective depletion voltage (EDV) defined as voltage at which 80% of charge is collected) is plotted against fluence for VELO sensors of various initial EDV. The EDV from data is compared to depletion voltages predicted by the Hamburg model [35], with good agreement observed prior to, and after sensor type-inversion. Figure taken from [133].

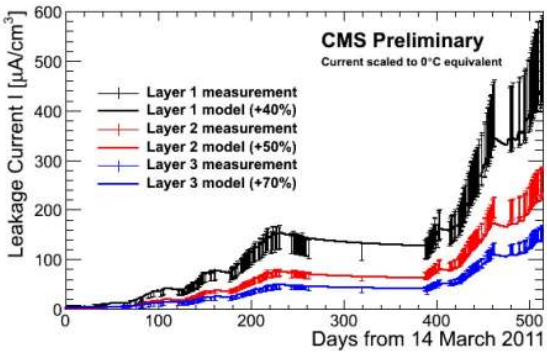

Fig. 35. Average leakage current in each CMS pixel barrel layer as a function of time in 2011 and 2012. The data are compared witha leakage current model from [35] and show good agreement [135]. Figure taken from [135].

The differences between data and simulation are typically less than 30%. The LHCb VELO collaboration reports a good agreement between the observed and modeled radiation damages in terms of increased leakage current, depletion voltage shift, and type inversion of the n-in-n sensors toward effectively n-in-p sensors (see Fig. 34 and [133], [134]). Fig. 35 shows the evolution with time of the leakage current in the CMS Barrel layers in comparison to the model in [135]. Data and model are agreeing well also in this case. In summary, a good agreement is found between the radiation damage models developed in the dedicated irradiation and characterization campaigns and the estimate of the fluence corresponding to given integrated luminosities and performed using the NIEL hypothesis. This promising result is now challenged against the strongly increasing cumulated luminosity in the very successful operation of the LHC machine in the years 2016 and 2017.

ACKNOWLEDGMENT

The author would like to thank the members of the RD50 collaboration as well to the chairs and copresenters of the RADECS short course for the opportunity to present this paper and for the very helpful comments and advice in preparing the lecture and the notes. A substantial part of the RADECS 2017 short course and this review paper are based on results originating from RD50 colleagues. It is a pleasure to work in a collaboration that is driven by the eagerness of the members to understand fundamental physics problems and to develop new (radiation tolerant) detector concepts in a friendly and pleasant atmosphere.

REFERENCES

[1] G. Apollinari *et al.*, "High-luminosity large hadron collider (HL-LHC): Technical design report v.0.1," CERN, Genève, Switzerland, Tech. Rep. CERN-2017-007-M, 2017.

[2] RD2 Collaboration, "R&D proposal," CERN, Genève, Switzerland, Tech. Rep. CERN/DRDC/90-27 and DRDC/P3, Aug. 1990.

[3] G. N. Taylor *et al.*, "Radiation induced bulk damage in silicon detectors," *Nucl. Instrum. Methods Phys. Res. A, Accel. Spectrom. Detect. Assoc. Equip.*, vol. 383, no. 1, pp. 144–154, 1996.

[4] RD48 Collaboration, "ROSE research and development on silicon for future experiments," CERN, Genève, Switzerland, Tech. Rep. LHCC 96-23 P62 and LHC R&D, Apr. 1996. [Online]. Available: http://www.cern.ch/rd48/

[5] RD50 Collaboration, "Radiation hard semiconductor devices for very high luminosity colliders," CERN, Genève, Switzerland, Tech. Rep. LHCC 2002-003 and LHCC P6, Feb. 2002. [Online]. Available: http://www.cern.ch/rd50/

[6] G. Kramberger, "Solid state detectors for high radiation environments," in *Landolt-Börnstein—Group I Elementary Particles, Nuclei and Atoms*, vol. 21B2. Berlin, Germany: Springer-Verlag, 2011.

[7] C. Leroy and P.-G. Rancoita, *Principles of Radiation Interaction in Matter and Detection*, 4th ed. Singapore: World Scientific, 2016.

[8] J. R. Srour and J. W. Palko, "Displacement damage effects in irradiated semiconductor devices," *IEEE Trans. Nucl. Sci.*, vol. 60, no. 3, pp. 1740–1766, Jun. 2013.

[9] F. Hartmann, *Evolution of Silicon Sensor Technology in Particle Physics*, 2nd ed. Berlin, Germany: Springer, 2017.

[10] *The High Luminosity LHC (HL-LHC) Project*. Accessed: Apr. 11, 2018. [Online]. Available: http://hilumilhc.web.cern.ch/about/hl-lhc-project

[11] LHCb Collaboration, "Framework TDR for the LHCb upgrade," CERN, Genève, Switzerland, Tech. Rep. CERN-LHCC-2012-007; LHCb-TDR-012, 2012.

[12] ALICE Collaboration, "Technical design report for the upgrade of the ALICE inner tracking system," CERN, Genève, Switzerland, Tech. Rep. CERN-LHCC-2013-024, 2013.

[13] ATLAS Collaboration, "ATLAS letter of intent phase-II upgrade," CERN, Genève, Switzerland, Tech. Rep. CERN-2012-022; LHCC-I-023, 2012.

[14] ATLAS Collaboration, "Technical design report for the ATLAS inner tracker strip detector," CERN, Genève, Switzerland, Tech. Rep. CERN-LHCC-2017-005; ATLAS-TDR-025, 2017.

[15] ATLAS Collaboration, "Technical design report for the ATLAS inner tracker pixel detector," CERN, Genève, Switzerland, Tech. Rep. CERN-LHCC-2017-021; ATLAS-TDR-030, 2017.

[16] CMS Collaboration, "Technical proposal for the phase-II upgrade of the CMS detector," CERN, Genève, Switzerland, Tech. Rep. CERN-LHCC-2015-010; LHCC-P-008; CMS-TDR-15-02, Jun. 2015.

[17] CMS Collaboration, "The phase-2 upgrade of the CMS tracker," CERN, Genève, Switzerland, Tech. Rep. CERN-LHCC-2017-009; CMS-TDR-014, 2017.

[18] CMS Collaboration, "The phase-2 upgrade of the CMS endcap calorimeter," CERN, Genève, Switzerland, Tech. Rep. CERN-LHCC-2017-023; CMS-TDR-17-007, 2017.

[19] P. S. Miyagawa and I. Dawson, "Radiation background studies for the phase II inner tracker upgrade," CERN, Genève, Switzerland, Tech. Rep. ATL-UPGRADE-PUB-2014-003, Sep. 2014.

[20] M. Benedikt and F. Zimmermann, "Towards future circular colliders," *J. Korean Phys. Soc.*, vol. 69, no. 6, pp. 893–902, Sep. 2016.

[21] M. I. Besana, F. Cerutti, A. Ferrari, W. Riegler, and V. Vlachoudis, "Evaluation of the radiation field in the future circular collider detector," *Phys. Rev. Accel. Beams*, vol. 19, p. 111004, Nov. 2016.

[22] A. Vasilescu and G. Lindstroem. *Displacement Damage in Silicon*. Accessed: Apr. 11, 2018. [Online]. Available: http://www.cern.ch/rd50/

[23] G. P. Summers, E. A. Burke, P. Shapiro, R. J. Walters, and S. R. Messenger, "Damage correlations in semiconductors exposed to gamma, electron and proton radiations," *IEEE Trans. Nucl. Sci.*, vol. 40, no. 6, pp. 1372–1379, Dec. 1993.

[24] M. Huhtinen and P. Aarnio, "Pion induced displacement damage in silicon devices," *Nucl. Instrum. Methods Phys. Res. A, Accel. Spectrom. Detect. Assoc. Equip.*, vol. 335, no. 3, pp. 580–582, 1993.

[25] P. J. Griffin, "SNL RML recommended. Dosimetry cross section compendium," Sandia Nat. Lab., Livermore, CA, USA, Tech. Rep. SAND92-0094, 1993.

[26] A. Y. Konobeyev, Y. A. Korovin, and V. N. Sosnin, "Neutron displacement cross-sections for structural materials below 800 MeV," *J. Nucl. Mater.*, vol. 186, no. 2, pp. 117–130, 1992.

[27] M. Huhtinen, "Simulation of non-ionising energy loss and defect formation in silicon," *Nucl. Instrum. Methods Phys. Res. A, Accel. Spectrom. Detect. Assoc. Equip.*, vol. 491, pp. 194–215, Sep. 2002.

[28] C. Inguimbert, P. Arnolda, T. Nuns, and G. Rolland, "'Effective NIEL' in silicon: Calculation using molecular dynamics simulation results," *IEEE Trans. Nucl. Sci.*, vol. 57, no. 4, pp. 1915–1923, Aug. 2010.

[29] C. Inguimbert and S. Messenger, "Equivalent displacement damage dose for on-orbit space applications," *IEEE Trans. Nucl. Sci.*, vol. 59, no. 6, pp. 3117–3125, Dec. 2012.

[30] S. R. Messenger, G. P. Summers, E. A. Burke, R. J. Walters, and M. A. Xapsos, "Modeling solar cell degradation in space: A comparison of the NRL displacement damage dose and the JPL equivalent fluence approaches," *Progr. Photovoltaics, Res. Appl.*, vol. 9, no. 2, pp. 103–121, 2001. [Online]. Available: http://dx.doi.org/10.1002/pip.357

[31] S. R. Messenger *et al.*, "Correlation of telemetered solar array data with particle detector data on GPS spacecraft," *IEEE Trans. Nucl. Sci.*, vol. 58, no. 6, pp. 3118–3125, Dec. 2011.

[32] R. Radu, I. Pintilie, L. C. Nistor, E. Fretwurst, G. Lindstroem, and L. F. Makarenko, "Investigation of point and extended defects in electron irradiated silicon-dependence on the particle energy," *J. Appl. Phys.*, vol. 117, no. 16, p. 164503, 2015.

[33] S. M. Sze, *Semiconductor Devices, Physics and Technology*, 2nd ed. Hoboken, NJ, USA: Wiley, 2002, ch. 3.

[34] M. Moll, E. Fretwurst, and G. Lindström, "Leakage current of hadron irradiated silicon detectors—Material dependence," *Nucl. Instrum. Methods Phys. Res. A, Accel. Spectrom. Detect. Assoc. Equip.*, vol. 426, pp. 87–93, Apr. 1999.

[35] M. Moll, "Radiation damage in silicon particle detectors: Microscopic defects and macroscopic properties," Ph.D. dissertation, Dept. Phys., Univ. Hamburg, Hamburg, Germany, 1999.

[36] I. Pintilie, E. Fretwurst, G. Lindström, and J. Stahl, "Results on defects induced by ^{60}Co gamma irradiation in standard and oxygen-enriched silicon," *Nucl. Instrum. Methods Phys. Res. A, Accel. Spectrom. Detect. Assoc. Equip.*, vol. 514, pp. 18–24, 2003.

[37] I. Pintilie, G. Lindstroem, A. Junkes, and E. Fretwurst, "Radiation-induced point- and cluster-related defects with strong impact on damage properties of silicon detectors," *Nucl. Instrum. Methods Phys. Res. A, Accel. Spectrom. Detect. Assoc. Equip.*, vol. 611, pp. 52–68, Jun. 2009.

[38] A. Chilingarov, "Temperature dependence of the current generated in Si bulk," *J. Instrum.*, vol. 8, no. 10, p. P10003, 2013.

[39] M. Moll, E. Fretwurst, M. Kuhnke, and G. Lindström, "Relation between microscopic defects and macroscopic changes in silicon detector properties after hadron irradiation," *Nucl. Instrum. Methods Phys. Res. B, Beam Interact. Mater. At.*, vol. 186, pp. 100–110, Jan. 2002.

[40] V. Eremin, E. Verbitskaya, and Z. Li, "The origin of double peak electric field distribution in heavily irradiated silicon detectors," *Nucl. Instrum. Methods Phys. Res. A, Accel. Spectrom. Detect. Assoc. Equip.*, vol. 476, no. 3, pp. 556–564, 2002.

[41] D. Campbell, A. Chilingarov, and T. Sloan, "Frequency and temperature dependence of the depletion voltage from CV measurements for irradiated SI detectors," *Nucl. Instrum. Methods Phys. Res. A, Accel. Spectrom. Detect. Assoc. Equip.*, vol. 492, pp. 402–410, Oct. 2002.

[42] R. Wunstorf, "Systematische untersuchungen zur strahlenresistenz von silizium-detektoren für die verwendung in hochenergiephysik-experiment en," Ph.D. dissertation, Dept. Phys., Univ. Hamburg, Hamburg, Germany, 1992.

[43] G. Lindström *et al.*, "Radiation tolerance of epitaxial silicon detectors at very large proton fluences," *Nucl. Instrum. Methods Phys. Res. A, Accel. Spectrom. Detect. Assoc. Equip.*, vol. 556, no. 2, pp. 451–458, 2006.

[44] N. Pacifico, I. D. Kittelmann, M. Fahrer, M. Moll, and O. Militaru, "Characterization of proton and neutron irradiated low resistivity p-on-n magnetic czochralski ministrip sensors and diodes," *Nucl. Instrum. Methods Phys. Res. A, Accel. Spectrom. Detect. Assoc. Equip.*, vol. 658, no. 1, pp. 55–60, 2011.

[45] G. Lindström *et al.*, "Radiation hard silicon detectors—Developments by the RD48 (ROSE) collaboration," *Nucl. Instrum. Methods Phys. Res. A, Accel. Spectrom. Detect. Assoc. Equip.*, vol. 466, no. 2, pp. 308–326, 2001.

[46] M. Moll, E. Fretwurst, and G. Lindström, "Investigation on the improved radiation hardness of silicon detectors with high oxygen concentration," *Nucl. Instrum. Methods Phys. Res. A, Accel. Spectrom. Detect. Assoc. Equip.*, vol. 439, pp. 282–292, Jan. 2000.

[47] A. Ruzin, "Recent results from the RD-48 (ROSE) collaboration," *Nucl. Instrum. Methods Phys. Res. A, Accel. Spectrom. Detect. Assoc. Equip.*, vol. 447, pp. 116–125, Jun. 2000.

[48] K. Kaska, "Characterization of radiation damage in detectors made from different silicon materials," Ph.D. dissertation, Faculty Phys., Tech. Univ. Wien, Wien, Austria, 2014.

[49] A. Affolder *et al.*, "Charge collection studies in irradiated HV-CMOS particle detectors," *J. Instrum.*, vol. 11, no. 4, p. P04007, 2016.

[50] E. Cavallaro *et al.*, "Studies of irradiated AMS H35 CMOS detectors for the atlas tracker upgrade," *J. Instrum.*, vol. 12, no. 01, p. C01074, 2017.

[51] B. Hiti *et al.*, "Charge collection properties in an irradiated pixel sensor built in a thick-film HV-SOI process," *J. Instrum.*, vol. 12, no. 10, p. P10020, 2017.

[52] I. Mandić *et al.*, "Neutron irradiation test of depleted CMOS pixel detector prototypes," *J. Instrum.*, vol. 12, no. 2, p. P02021, 2017.

[53] P. D. de Almeida, "Measurement of the acceptor removal rate in silicon pad diodes," presented at the 30th RD50 Workshop Radiat. Semiconductor Devices Frovery High Luminosity Colliders, Krakow, Poland, Jun. 2017, [Online]. Available: https://indico.cern.ch/event/637212/

[54] G. Kramberger, "Overview of sensor radiation tolerance at HL-LHC levels," presented at the 11th Int. Hiroshima Symp. Develop. Appl. Semiconductor Track. Detectors, Okinawa, Japan, Dec. 2017. [Online]. Available: https://indico.cern.ch/event/577879/

[55] R. Wunstorf, W. M. Bugg, J. Walter, F. W. Garber, and D. Larson, "Investigations of donor and acceptor removal and long term annealing in silicon with different boron/phosphorus ratios," *Nucl. Instrum. Methods Phys. Res. A, Accel. Spectrom. Detect. Assoc. Equip.*, vol. 377, pp. 228–233, Aug. 1996.

[56] O. Krasel, C. Gossling, R. Klingenberg, S. Rajek, and R. Wunstorf, "Measurement of trapping time constants in proton-irradiated silicon pad detectors," *IEEE Trans. Nucl. Sci.*, vol. 51, no. 6, pp. 3055–3062, Dec. 2004.

[57] G. Kramberger, V. Cindro, I. Mandić, M. Mikuž, and M. Zavrtanik, "Effective trapping time of electrons and holes in different silicon materials irradiated with neutrons, protons and pions," *Nucl. Instrum. Methods Phys. Res. A, Accel. Spectrom. Detect. Assoc. Equip.*, vol. 481, pp. 297–305, Apr. 2002.

[58] A. G. Bates and M. Moll, "A comparison between irradiated magnetic Czochralski and float zone silicon detectors using the transient current technique," *Nucl. Instrum. Methods Phys. Res. A, Accel. Spectrom. Detect. Assoc. Equip.*, vol. 555, pp. 113–124, Dec. 2005.

[59] J. Lange, J. Becker, D. Eckstein, E. Fretwurst, R. Klanner, and G. Lindström, "Charge collection studies of proton-irradiated n- and p-type epitaxial silicon detectors," *Nucl. Instrum. Methods Phys. Res. A, Accel. Spectrom. Detect. Assoc. Equip.*, vol. 624, pp. 405–409, Jun. 2010.

[60] W. Adam *et al.*, "Trapping in proton irradiated p^+-n-n^+ silicon sensors at fluences anticipated at the HL-LHC outer tracker," *J. Instrum.*, vol. 11, no. 4, p. P04023, 2016.

[61] G. Kramberger, "Signal development in irradiated silicon detectors," Ph.D. dissertation, Faculty Math. Phys., Univ. Ljubljana, Ljubljana, Slovenia, 1998.

[62] J. Weber and R. Klingenberg, "Free charge carriers trapping properties in neutron-irradiated DOFZ silicon pad detectors," *IEEE Trans. Nucl. Sci.*, vol. 54, no. 6, pp. 2701–2705, Dec. 2007.

[63] V. Eremin, N. Strokan, E. Verbitskaya, and Z. Li, "Development of transient current and charge techniques for the measurement of effective net concentration of ionized charges (N_{eff}) in the space charge region of p-n junction detectors," *Nucl. Instrum. Methods Phys. Res. A, Accel. Spectrom. Detect. Assoc. Equip.*, vol. 372, no. 3, pp. 388–398, 1996.

[64] G. Kramberger *et al.*, "Investigation of irradiated silicon detectors by edge-TCT," *IEEE Trans. Nucl. Sci.*, vol. 57, no. 4, pp. 2294–2302, Aug. 2010.

[65] M. F. García *et al.*, "On the determination of the substrate effective doping concentration of irradiated HV-CMOS sensors using an edge-TCT technique based on the two-photon-absorption process," *J. Instrum.*, vol. 12, no. 1, p. C01038, 2017.

[66] G. Kramberger, V. Cindro, I. Mandić, M. Mikuž, M. Milovanović, and M. Zavrtanik, "Modeling of electric field in silicon micro-strip detectors irradiated with neutrons and pions," *J. Instrum.*, vol. 9, no. 10, p. P10016, 2014.

[67] H. Spieler, *Semiconductor Detector Systems*. New York, NY, USA: Oxford Univ. Press, 2015.

[68] E. Fischer, L. Rossi, N. Wermes, and T. Rohe, *Pixel Detectors—From Fundamentals to Applications*. Berlin, Germany: Springer, 2006.

[69] W. Shockley, "Currents to conductors induced by a moving point charge," *J. Appl. Phys.*, vol. 9, no. 10, pp. 635–636, 1938.

[70] S. Ramo, "Currents induced by electron motion," *Proc. IRE*, vol. 27, no. 9, pp. 584–585, Sep. 1939.

[71] M. Moll, "Recent advances in the development of radiation tolerant silicon detectors for the super-LHC," in *Astroparticle, Particle and Space Physics, Detectors and Medical Physics Applications*. Singapore: World Scientific, 2011, pp. 101–110.

[72] A. Affolder, P. Allport, and G. Casse, "Charge collection efficiencies of planar silicon detectors after reactor neutron and proton doses up to 1.6×10^{16} $n_{eq}cm^{-2}$," *Nucl. Instrum. Methods Phys. Res. A, Accel. Spectrom. Detect. Assoc. Equip.*, vol. 612, pp. 470–473, Jan. 2010.

[73] A. Affolder, P. Allport, and G. Casse, "Collected charge of planar silicon detectors after pion and proton irradiations up to 2.2×10^{16} $n_{eq}cm^{-2}$," *Nucl. Instrum. Methods Phys. Res. A, Accel. Spectrom. Detect. Assoc. Equip.*, vol. 623, no. 1, pp. 177–179, 2010.

[74] W. Adam *et al.*, "P-type silicon strip sensors for the new CMS Tracker at HL-LHC," *J. Instrum.*, vol. 12, no. 6, p. P06018, 2017.

[75] G. Casse, A. Affolder, P. Allport, H. Brown, and M. Wormald, "Enhanced efficiency of segmented silicon detectors of different thicknesses after proton irradiations up to $1\times10^{16}n_{eq}$ cm^{-2}," *Nucl. Instrum. Methods Phys. Res. A, Accel. Spectrom. Detect. Assoc. Equip.*, vol. 624, no. 2, pp. 401–404, 2010.

[76] S. Terzo *et al.*, "Heavily irradiated n-in-p thin planar pixel sensors with and without active edges," *J. Instrum.*, vol. 9, no. 5, p. C05023, 2014.

[77] G. Casse, P. Allport, and A. Watson, "Effects of accelerated annealing on p-type silicon micro-strip detectors after very high doses of proton irradiation," *Nucl. Instrum. Methods Phys. Res. A, Accel. Spectrom. Detect. Assoc. Equip.*, vol. 568, no. 1, pp. 46–50, 2006.

[78] I. Mandić *et al.*, "Accelerated annealing of n^+-p strip detectors irradiated with pions," *J. Instrum.*, vol. 6, no. 11, p. P11008, 2011.

[79] S. I. Parker, C. J. Kenney, and J. Segal, "3D—A proposed new architecture for solid-state radiation detectors," *Nucl. Instrum. Methods Phys. Res. A, Accel. Spectrom. Detect. Assoc. Equip.*, vol. 395, no. 3, pp. 328–343, 1997.

[80] M. Mathes *et al.*, "Test beam characterization of 3-D silicon pixel detectors," *IEEE Trans. Nucl. Sci.*, vol. 55, no. 6, pp. 3731–3735, Dec. 2008.

[81] J. Lange *et al.*, "3D silicon pixel detectors for the high-luminosity LHC," *J. Instrum.*, vol. 11, no. 11, p. C11024, 2016.

[82] A. Zoboli *et al.*, "Double-sided, double-type-column 3-D detectors: Design, fabrication, and technology evaluation," *IEEE Trans. Nucl. Sci.*, vol. 55, no. 5, pp. 2775–2784, Oct. 2008.

[83] G. Pellegrini, M. Lozano, M. Ullán, R. Bates, C. Fleta, and D. Pennicard, "First double-sided 3-D detectors fabricated at CNM-IMB," *Nucl. Instrum. Methods Phys. Res. A, Accel. Spectrom. Detect. Assoc. Equip.*, vol. 592, pp. 38–43, Jul. 2008.

[84] ATLAS Collaboration, "ATLAS insertable b-layer technical design report addendum," CERN, Genève, Switzerland, Tech. Rep. CERN-LHCC-2012-009; ATLAS-TDR-19-ADD-1, 2012.

[85] I. Pintilie, L. Nistor, S. Nistor, and A. Joita, "Experimental techniques for defect characterization of highly irradiated materials and structures," in *Proc. Sci. PoS*, 2016, pp. 1–12.

[86] D. V. Lang, "Deep-level transient spectroscopy: A new method to characterize traps in semiconductors," *J. Appl. Phys.*, vol. 45, no. 7, pp. 3023–3032, Jul. 1974.

[87] J.-M. Spaeth and H. Overhof, *Point Defects in Semiconductors and Insulators*. Berlin, Germany: Springer, 2003.

[88] A. Junkes, "Status of defect investigations," in *Proc. Sci. PoS*, 2011, pp. 1–13.

[89] I. Pintilie, E. Fretwurst, and G. Lindström, "Cluster related hole traps with enhanced-field-emission—The source for long term annealing in hadron irradiated Si diodes," *Appl. Phys. Lett.*, vol. 92, no. 2, p. 024101, 2008.

[90] I. Pintilie, M. Buda, E. Fretwurst, G. Lindström, and J. Stahl, "Stable radiation-induced donor generation and its influence on the radiation tolerance of silicon diodes," *Nucl. Instrum. Methods Phys. Res. A, Accel. Spectrom. Detect. Assoc. Equip.*, vol. 556, no. 1, pp. 197–208, 2006.

[91] E. Fretwurst, F. Hönniger, G. Kramberger, G. Lindström, I. Pintilie, and R. Röder, "Radiation damage studies on MCz and standard and oxygen enriched epitaxial silicon devices," *Nucl. Instrum. Methods Phys. Res. A, Accel. Spectrom. Detect. Assoc. Equip.*, vol. 583, no. 1, pp. 58–63, 2007.

[92] I. Pintilie, E. Fretwurst, G. Lindström, and J. Stahl, "Close to midgap trapping level in ^{60}Co gamma irradiated silicon detectors," *Appl. Phys. Lett.*, vol. 81, no. 1, pp. 165–167, 2002.

[93] I. Pintilie, E. Fretwurst, G. Lindström, and J. Stahl, "Second-order generation of point defects in gamma-irradiated float-zone silicon, an explanation for 'type inversion,"' *Appl. Phys. Lett.*, vol. 82, no. 13, pp. 2169–2171, 2003.

[94] R. M. Fleming, C. H. Seager, D. V. Lang, E. Bielejec, and J. M. Campbell, "Defect-driven gain bistability in neutron damaged, silicon bipolar transistors," *Appl. Phys. Lett.*, vol. 90, no. 17, p. 172105, 2007.

[95] V. P. Markevich *et al.*, "Trivacancy and trivacancy-oxygen complexes in silicon: Experiments and ab *initio* modeling," *Phys. Rev. B, Condens. Matter*, vol. 80, p. 235207, Dec. 2009.

[96] A. Junkes, D. Eckstein, I. Pintilie, L. F. Makarenko, and E. Fretwurst, "Annealing study of a bistable cluster defect," *Nucl. Instrum. Methods Phys. Res. A, Accel. Spectrom. Detect. Assoc. Equip.*, vol. 612, no. 3, pp. 525–529, 2010.

[97] J. Coutinho *et al.*, "Electronic and dynamical properties of the silicon trivacancy," *Phys. Rev. B, Condens. Matter*, vol. 86, p. 174101, Nov. 2012.

[98] V. P. Markevich, A. R. Peaker, B. Hamilton, S. B. Lastovskii, and L. I. Murin, "Donor levels of the divacancy-oxygen defect in silicon," *J. Appl. Phys.*, vol. 115, no. 1, p. 012004, 2014.

[99] M. Moll, H. Feick, E. Fretwurst, and G. Lindström, "Correlation between a deep hole trap and the reverse annealing effect in neutron-irradiated silicon detectors," *Nucl. Instrum. Methods Phys. Res. A, Accel. Spectrom. Detect. Assoc. Equip.*, vol. 409, pp. 194–197, May 1998.

[100] P. M. Mooney, L. J. Cheng, M. Süli, J. D. Gerson, and J. W. Corbett, "Defect energy levels in boron-doped silicon irradiated with 1-MeV electrons," *Phys. Rev. B, Condens. Matter*, vol. 15, pp. 3836–3843, Apr. 1977.

[101] L. F. Makarenko, S. B. Lastovskii, F. P. Korshunov, M. Moll, I. Pintilie, and N. V. Abrosimov, "Formation and annealing of boron-oxygen defects in irradiated silicon and silicon-germanium n^+-p structures," *AIP Conf.*, vol. 1583, no. 1, pp. 123–126, 2014.

[102] L. F. Makarenko, S. B. Lastovskii, H. S. Yakushevich, M. Moll, and I. Pintilie, "Forward current enhanced elimination of the radiation induced boron-oxygen complex in silicon n^+-p diodes," *Phys. Status Solidi A*, vol. 211, no. 11, pp. 2558–2562, 2014.

[103] L. F. Makarenko, S. B. Lastovskii, H. S. Yakushevich, M. Moll, and I. Pintilie, "Effect of electron injection on defect reactions in irradiated silicon containing boron, carbon, and oxygen," *J. Appl. Phys.*, vol. 123, no. 16, p. 161576, 2018.

[104] M. Moll, H. Feick, E. Fretwurst, G. Lindström, and C. Schütze, "Comparison of defects produced by fast neutrons and ^{60}Co-gammas in high-resistivity silicon detectors using deep-level transient spectroscopy," *Nucl. Instrum. Methods Phys. Res. A, Accel. Spectrom. Detect. Assoc. Equip.*, vol. 388, pp. 335–339, Jun. 1997.

[105] R. Radu, E. Fretwurst, R. Klanner, G. Lindstroem, and I. Pintilie, "Radiation damage in n-type silicon diodes after electron irradiation with energies between 1.5 MeV and 15 MeV," *Nucl. Instrum. Methods Phys. Res. A, Accel. Spectrom. Detect. Assoc. Equip.*, vol. 730, pp. 84–90, Dec. 2013.

[106] B. Svensson, B. Mohadjeri, A. Hallen, J. Svensson, and J. Corbett, "Divacancy acceptor levels in ion-irradiated silicon," *Phys. Rev. B, Condens. Matter*, vol. 43, no. 3, p. 2292, Jan. 1991.

[107] M. Kuhnke, "Microscopic investigations on various silicon materials irradiated with different particles with the DLTS method," Ph.D. dissertation, Dept. Phys., Univ. Hamburg, Hamburg, Germany, 2001.

[108] T. Peltola, "Simulation of radiation-induced defects," in *Proc. Sci. PoS*, 2015, p. 31.

[109] M. Petasecca, F. Moscatelli, D. Passeri, and G. U. Pignatel, "Numerical simulation of radiation damage effects in p-type and n-type FZ silicon detectors," *IEEE Trans. Nucl. Sci.*, vol. 53, no. 5, pp. 2971–2976, Oct. 2006.

[110] D. Pennicard *et al.*, "Simulations of radiation-damaged 3D detectors for the Super-LHC," *Nucl. Instrum. Methods Phys. Res. A, Accel. Spectrom. Detect. Assoc. Equip.*, vol. 592, pp. 16–25, Jul. 2008.

[111] R. Eber, "Investigations of new sensor designs and development of an effective radiation damage model for the simulation of highly irradiated silicon particle detectors," Ph.D. dissertation, Faculty Phys., Karlsruhe Inst. Technol., Karlsruhe, Germany, 2001.

[112] R. Dalal, A. Bhardwaj, K. Ranjan, K. Lalwani, and G. Jain, "Simulation of irradiated Si detectors," in *Proc. Sci. PoS*, 2014.

[113] F. Moscatelli, D. Passeri, A. Morozzi, G.-F. Dalla Betta, R. Mendicino, and G. M. Bilei, "Combined bulk and surface radiation damage effects at very high fluences in silicon detectors: Measurements and TCAD simulations," *IEEE Trans. Nucl. Sci.*, vol. 63, no. 5, pp. 2716–2723, Oct. 2016.

[114] R. Dalal, A. Bhardwaj, K. Ranjan, M. Moll, and A. Elliott-Peisert, "Combined effect of bulk and surface damage on strip insulation properties of proton irradiated n^+-p silicon strip sensors," *J. Instrum.*, vol. 9, no. 4, p. P04007, 2014.

[115] T. Peltola *et al.*, "A method to simulate the observed surface properties of proton irradiated silicon strip sensors," *J. Instrum.*, vol. 10, no. 4, p. C04025, 2015.

[116] *Microsoft Excel Software*. Accessed: Apr. 11, 2018. [Online]. Available: https://www.microsoft.com

[117] Synopsys Inc. *Synopsys Sentaurus Device Simulator*. Accessed: Apr. 11, 2018. [Online]. Available: https://www.synopsys.com

[118] Silvaco Inc. *Silvaco 2D and 3D Device Simulators*. Accessed: Apr. 11, 2018. [Online]. Available: https://www.silvaco.com

[119] J. Schwandt *et al.*, "Validation strategy for the simulation of highly irradiated pixel sensors," in *Proc. 11th Trento Workshop*, Feb. 2016, pp. 1–22. [Online]. Available: https://indico.cern.ch/event/452766/

[120] G. Pellegrini *et al.*, "Technology developments and first measurements of Low Gain Avalanche Detectors (LGAD) for high energy physics applications," *Nucl. Instrum. Methods Phys. Res. A, Accel. Spectrom. Detect. Assoc. Equip.*, vol. 765, pp. 12–16, Nov. 2014.

[121] G. Pellegrini *et al.*, "Recent technological developments on LGAD and iLGAD detectors for tracking and timing applications," *Nucl. Instrum. Methods Phys. Res. A, Accel. Spectrom. Detect. Assoc. Equip.*, vol. 831, pp. 24–28, Sep. 2016.

[122] H. F.-W. Sadrozinski, A. Seiden, and N. Cartiglia, "4D tracking with ultra-fast silicon detectors," *Rep. Progr. Phys.*, vol. 81, no. 2, p. 026101, 2018.

[123] G. Kramberger *et al.*, "Radiation effects in Low Gain Avalanche Detectors after hadron irradiations," *J. Instrum.*, vol. 10, no. 7, p. P07006, 2015.

[124] C. Gallrapp *et al.*, "Study of gain homogeneity and radiation effects of low gain avalanche pad detectors," *Nucl. Instrum. Methods Phys. Res. A, Accel. Spectrom. Detect. Assoc. Equip.*, vol. 875, pp. 27–34, Dec. 2017.

[125] R. Dalal, G. Jain, A. Bhardwaj, and K. Ranjan, "TCAD simulation of Low Gain Avalanche Detectors," *Nucl. Instrum. Methods Phys. Res. A, Accel. Spectrom. Detect. Assoc. Equip.*, vol. 836, pp. 113–121, Nov. 2016.

[126] E. Verbitskaya, V. Eremin, A. Zabrodskii, and P. Luukka, "Simulation of low gain avalanche detector characteristics based on the concept of negative feedback in irradiated silicon detectors with carrier impact ionization," *J. Instrum.*, vol. 11, no. 12, p. P12012, 2016.

[127] I. Perić, "A novel monolithic pixelated particle detector implemented in high-voltage CMOS technology," *Nucl. Instrum. Methods Phys. Res. A, Accel. Spectrom. Detect. Assoc. Equip.*, vol. 582, no. 3, pp. 876–885, 2007.

[128] M. Garcia-Sciveres and N. Wermes, "A review of advances in pixel detectors for experiments with high rate and radiation," *Rep. Progr. Phys.*, 2018. [Online]. Available: http://iopscience.iop.org/article/10.1088/1361-6633/aab064

[129] F. Hartmann, "Evolution of silicon parameters due to irradiation at the LHC," in *Proc. PoS*, 2011, pp. 1–10.

[130] R. Harper, "Radiation damage studies of the silicon microstrip detectors and finding an intermediate mass higgs boson at ATLAS," Ph.D. dissertation, Univ. Sheffield, Sheffield, U.K., 2001.

[131] O. Krasel, "Charge collection in irradiated silicon-detectors," Ph.D. dissertation, Dept. Phys., Univ. Dortmund, Dortmund, Germany, 2004.

[132] The ATLAS collaboration, "Operation and performance of the ATLAS semiconductor tracker," *J. Instrum.*, vol. 9, no. 8, p. P08009, 2014.

[133] A. Affolder *et al.*, "Radiation damage in the LHCb vertex locator," *J. Instrum.*, vol. 8, no. 8, p. P08002, 2013.

[134] J. Harrison and A. Webber, "Radiation damage in the LHCb VELO," *Nucl. Instrum. Methods Phys. Res. A, Accel. Spectrom. Detect. Assoc. Equip.*, vol. 699, pp. 193–197, Aug. 2013.

[135] S. Zenz, "Operational issues of the present CMS pixel detector," in *Proc. Sci. PoS*, 2012, pp. 1–9.